



Reversed, suppressed and layered granular segregation at large particle size ratios

Philip G. Gamble¹ , Jamie P. Webb¹ , J.M.N.T. Gray¹  and
Chris G. Johnson¹ 

¹Department of Mathematics and Manchester Centre for Nonlinear Dynamics, University of Manchester, Oxford Road, Manchester M13 9PL, UK

Corresponding author: Chris G. Johnson, chris.johnson@manchester.ac.uk

(Received 10 September 2025; revised 16 December 2025; accepted 22 January 2026)

Particle size segregation is a common occurrence in sheared granular flows under gravity. Segregation of size-bidisperse grain mixtures at size ratios of three or less has been extensively studied, but comparatively little is known about segregation of grains with more widely varying sizes, despite their relevance to natural and industrial flows. At larger size ratios the segregation behaviour of bidisperse mixtures may change drastically, including reversal of the direction of segregation, which no existing continuum model accounts for. This paper investigates the segregation behaviour of bidisperse granular mixtures up to a size ratio of seven and formulates a new continuum model for size segregation that captures the observed suppression and reversal of segregation. Discrete element method (DEM) simulations of flows on an inclined plane show a reversal of behaviour as the volume fraction of small particles increases, from states where the large particles rise to the free surface to states where they sink. At intermediate small-particle volume fractions, segregation is significantly reduced or even entirely absent, leading to well-mixed flows. In addition, a striking layering effect is observed at large size ratios, where large particles organise into distinct layers one particle thick, separated by thin bands of small particles. This layering is demonstrated both in simulations and, for the first time, in laboratory experiments. The continuum segregation model introduces a new bidirectional segregation flux that accounts for the reversal in segregation. The model is in good quantitative agreement with DEM simulations across a range of small-particle volume fractions.

Key words: avalanches, dry granular material

1. Introduction

Shearing of a granular material composed of particles of different sizes commonly leads to size segregation, where particles of different sizes migrate relative to each other within the flow. This results in a spatially inhomogeneous distribution of the material. Size segregation has major implications in both natural and industrial contexts. In geophysical mass flows such as avalanches and debris flows, it is thought to play a key role in the formation of static levees that can channelise the flow and significantly increase its runout distance (Iverson & Vallance 2001; Félix & Thomas 2004a; Johnson *et al.* 2012; Rocha, Johnson & Gray 2019). In industry, segregation presents a serious challenge by reducing the uniformity of mixtures and compromising product quality (Santl *et al.* 2012). Changes to both the industrial process and the particle composition are often needed to reduce the effects of segregation to acceptable levels (Schulze 2008).

In dense granular avalanches, the large particles usually (though not always) rise to the surface of the flow, as the small particles migrate down towards the base. Several views have been proposed on the underlying mechanism for this phenomenon. Middleton (1970) suggested that gaps form within the sheared granular material, into which smaller particles preferentially fall, as they are more likely to fit than larger ones (kinetic sieving). This results in a net downward flux of small particles, which, due to mass conservation, is balanced by a corresponding upward flux of large particles, known as squeeze expulsion (Savage & Lun 1988). Much recent work has moved towards describing segregation in terms of the differing response of large and small particles to gradients of pressure, shear stress and/or shear rate within a flow, and a resulting segregation force acting on particles (e.g. Gray & Thornton 2005; Fan & Hill 2011; Guillard, Forterre & Pouliquen 2016). At the grain scale, these forces, and their dependence on particle size and small-particle volume fraction, may depend on partitioning of stress between large and small grains, and the statistics of the void space surrounding them (Golick & Daniels 2009). Regardless of mechanism, the result is usually that large particles rise relative to small particles.

However, segregation behaves very differently in size-bidisperse mixtures at large particle size ratios, where the particle size ratio is defined as $R = d^l/d^s$, with d^l and d^s being the diameters of the large and small grains, respectively. For $R \gtrsim 4$ isolated large particles (intruders) sink towards the base of free-surface flows composed of otherwise monodisperse small particles of the same density, in both experiments (Thomas 2000; Félix & Thomas 2004b; Fraysse, D'Ortona & Thomas 2024) and discrete element method (DEM) simulations (Thomas & D'Ortona 2018; Jing *et al.* 2020, 2021). This is a robust effect in free-surface flows, occurring in chute flows, rotating drums and heap flows (Thomas & D'Ortona 2018). Moreover it occurs across a wide range of inertial numbers characteristic of the dense inertial regime (Jing *et al.* 2020). This effect has been termed reverse segregation in contrast to the conventional case, where large particles rise to the surface (Thomas 2000). Isolated large intruders may segregate to an intermediate position within a granular layer (Félix & Thomas 2004b; Thomas & D'Ortona 2018).

Reverse segregation of intruders is well established in free-surface flows but it is not universal across all flow configurations; it may be affected by the flow geometry, proximity to boundaries and interstitial fluid. In wall-driven flows, the segregation force due to gradients of shear rate may exceed that due to gravity, thereby suppressing reverse segregation (Jing *et al.* 2021). In oscillating shear cell experiments, Trehwela, Ancy & Gray (2021) did not observe reverse segregation of an intruder up to $R = 4.2$, which is close to the value at which Thomas (2000) reported it. However, the horizontal width of their shear cell is less than three large-particle diameters for $R = 4.2$, meaning wall effects may have been significant. Rousseau, Chauchat & Frey (2022) also did not report reverse

segregation up to $R = 5.2$ in turbulent bedload transport. This paper is focused primarily on dry inclined-plane flows, where reverse segregation is consistently observed (Thomas 2000).

A possible explanation for reverse segregation involves the notion of an effective density difference. In a flow with a single large intruder surrounded by small particles of the same intrinsic density ρ_* , the intruder appears denser than its surrounding medium. This is because, over the length scale of a large particle, the surrounding medium consists of a mixture of both small particles and void space and therefore has density $\rho_*\Phi$, where Φ is the total solids volume fraction, approximately 0.6 in dense granular flows. Thus the intruder's higher effective density causes it to sink. This idea has been used to calculate the buoyancy-like force on intruders (e.g. van der Vaart *et al.* 2018) and is supported by the rotating drum experiments of Félix & Thomas (2004b), who showed that an increase in the size of the intruder has a similar effect to an increase in intruder density, with both promoting reverse segregation. Jing *et al.* (2020) used the concept of effective density to predict both the direction of segregation (i.e. whether large particles rise or sink) and the force acting on a single intruder across a range of size and density ratios, by making an analogy with the Archimedean buoyancy force in fluids. The direction of segregation for an intruder is determined by a balance between an upward size-corrected granular buoyancy force and the downward gravitational force.

At large size ratios, the direction of segregation is not only dependent on the size ratio itself but also on the volume fraction of small particles. In chute flow experiments, Thomas (2000) observed that for size ratios greater than five, flows composed of 10 % small particles formed a surface layer of large grains, whereas flows with 90 % small particles had a surface made entirely of small particles. This contrasts with the behaviour at lower size ratios ($R \leq 4$) where a layer of large particles formed at the surface for both 10 % and 90 % volume fractions of small particles. The observations of Thomas (2000) of the location of large and small particles within a bidisperse granular pile suggest that, for any fixed size ratio greater than five, a transition occurs between large particles rising and sinking as the volume fraction of small particles is increased. However, the behaviour of mixtures at intermediate volume fractions of small particles is much less well characterised than the intruder limits involving a few small or large intruders. In thick chute flows, the details of the transition between small and large particles at the surface and the variation of the mixture composition with depth remain poorly understood. Such information is vital in developing continuum models capable of predicting segregation over a range of small-particle volume fractions at large size ratios.

Continuum models have been successful in modelling segregation in size-bidisperse mixtures for size ratios $R \lesssim 3$, where large particles are concentrated at the surface of flows (Gray 2018; Umbanhower, Lueptow & Ottino 2019). However the physical mechanisms that cause large particles to be transported to the surface (e.g. Staron & Phillips 2015) do not control the segregation behaviour at larger R , where there may be a reversal in the direction of segregation, depending on the volume fraction of small particles. Existing continuum models do not account for this mechanism and their parameters, calibrated for small R , predict the wrong direction of segregation at larger R .

In the context of combined size and density segregation, models have been proposed that are capable of providing a transition between large particles sinking and rising (Tripathi & Khakar 2013; Tunuguntla, Bokhove & Thornton 2014; Gray & Ancey 2015; Duan *et al.* 2021). These models allow large particles to sink if they are denser than the small particles, but they do not describe reverse segregation due to size differences alone. Moreover, the empirical parameters in the size and density model of Duan *et al.* (2021) have only been calculated up to $R = 2$ which is below the value of $R \approx 4$ needed for purely size-driven

reverse segregation to occur (Thomas 2000). Current models are therefore limited in their applicability to $R \lesssim 4$.

The present study aims to address these shortcomings by first investigating the segregation behaviour of bidisperse mixtures at large particle size ratios and, subsequently, developing a continuum model for size segregation capable of capturing the observed phenomena, which are qualitatively different from those at smaller size ratios. To achieve this, the model introduces a new segregation flux which changes sign with the small-particle concentration. This is termed a bidirectional segregation flux and it accounts for the reversal in the direction of segregation at a fixed size ratio as the fraction of small particles increases. Predictions of the continuum model are then compared with steady-state DEM data on an inclined plane at $R = 3$ and $R = 6$ where it shows good quantitative agreement over a range of small-particle volume fractions. This includes accurately capturing new, approximately uniform states that emerge at $R = 6$ close to the transition between small and large particles being at the surface, where segregation is significantly reduced or even absent.

Another intriguing but largely unexplored phenomenon that occurs in bidisperse granular flows at large size ratios is the organisation of large particles into distinct layers. This layering has been noted in DEM simulations of bidisperse flows using periodic boundary conditions, in the configuration of an avalanche down an inclined plane with $R = 3.5$ (Tunuguntla, Thornton & Weinhart 2016), and bedload transport with $R = 4$ (Chassagne 2021). In both cases, large particles formed approximately four distinct layers, with each layer parallel to the free surface of the flow, and each layer a single large particle thick and separated by thin bands of small particles. However, remarkably little is known about the layering phenomenon, including whether it is associated with proximity to a rigid or free-surface boundary of the flow. Indeed, until now it has been unclear whether layering of this kind occurs in real granular flows, or whether it is an artefact of the periodic boundary conditions applied in numerical simulations. Like segregation, layering acts to separate an initially well-mixed flow into one with a spatially varying concentration of large and small particles; in this sense it could be considered as a form of segregation. However, the changes in concentration that result from layering occur only at the grain scale, unlike the effects of segregation, which occur over the entire depth of the flow, and this difference allows us to treat the two phenomena as distinct.

The main contributions of this paper are twofold. Firstly, a continuum segregation model is presented that captures the segregation behaviour of particles with $R \gtrsim 4$ in which the direction of segregation of large particles depends on their concentration. This model is in quantitative agreement with simulation results over the complete range of small-particle concentrations, successfully capturing states with large particles at the surface, small particles at the surface and states where segregation is strongly suppressed and the mixture composition is nearly homogeneous. Secondly, the first direct experimental observations of layering of size-bidisperse granular flows are provided. This is presented alongside numerical evidence that evinces the structure of the layering and supports the hypothesis that layering is an intrinsic behaviour of shearing size-bidisperse mixtures, and not a result of proximity to flow boundaries or numerical periodic boundary conditions.

The paper is organised as follows. Section 2 describes the methods used in DEM simulations of bidisperse inclined-plane flows and presents the observed segregation behaviour. Section 3 examines the layering observed in the simulations in both inclined-plane flow over a rough base and in simple shear flow in a fully periodic domain. The existence of these layers is then confirmed experimentally. The governing equations for the continuum segregation model are presented in §4, and the bidirectional segregation flux that captures the observed reversal of the segregation direction at large size ratios is

introduced in § 5. In § 6 the predictions of the continuum model are compared with the results of our DEM simulations and § 7 concludes.

2. Discrete element method simulations

2.1. Simulation methods

The segregation behaviours of size-bidisperse mixtures on an inclined plane are studied using DEM simulations using the open-source software LAMMPS (Thompson *et al.* 2022). Grains are simulated as spheres of intrinsic density ρ_* and diameters d^s and d^l for the small and large grains, respectively. The size ratio $R = d^l/d^s$ is in the range $2 \leq R \leq 7$ in this paper, with particular focus on the cases $R = 3$ and $R = 6$. To prevent crystallisation, each species of grain is given a 10 % polydispersity either side of their mean diameter d^v , with diameters uniformly distributed in the range $(0.9d^v, 1.1d^v)$. The particles are subject to gravitational acceleration g .

Contacts between particles are resolved using a linear spring–dashpot model with static friction (Cundall & Strack 1979). For the normal force, the coefficient of restitution is $\epsilon = 0.8$ and a fixed binary collision time of $t_c = 0.005(d^s/g)^{1/2}$ is used as in Tunuguntla, Weinhart & Thornton (2017). The normal spring stiffness k_n and normal viscoelastic damping constant γ_n can then be obtained from t_c and ϵ (e.g. Thornton *et al.* 2012). For the tangential force, the coefficient of friction is $\mu_c = 0.5$, the tangential stiffness is $k_t = 2/7k_n$ and the tangential viscoelastic damping coefficient is $\gamma_t = 0.5\gamma_n$. The simulation time step is $t_c/50$ to ensure numerical accuracy (Silbert *et al.* 2001).

The mixture flows down a rough plane inclined at angle θ to the horizontal. A Cartesian coordinate system is chosen with (x, y, z) denoting the down-slope, cross-slope and slope-normal directions, respectively. Periodic boundary conditions are enforced in the x and y directions. The results are independent of numerical domain size, verified by varying the size of the periodic box from $12d^l$ to $36d^l$ in x and $8d^l$ to $10d^l$ in y . This is $72d^s$ to $216d^s$ and $48d^s$ to $60d^s$ at size ratio $R = 6$. To minimise slip, the base is made rough by fixing a layer containing a mixture of small and large grains with the same frictional and material properties as those in the flow. This minimises slip at the base whilst also preventing the small particles from filling the base and thus being lost to the flow.

The small-particle fraction $\overline{\phi^s}$ is defined as the total volume of small particles divided by the total volume of granular material, and is varied between simulations. Since the intrinsic density of both species is the same, $\overline{\phi^s}$ is equivalent to the mass fraction of small particles. When $\overline{\phi^s} = 1$ the flow consists of entirely small particles, and when $\overline{\phi^s} = 0$ it corresponds to entirely large particles. Small-particle fractions in the range $0.1 \leq \overline{\phi^s} \leq 0.9$ are considered.

The initial condition consists a layer of small grains lying on top of a layer of large grains, with all grains initially at rest. The simulations are run until a statistically steady state is reached and the resulting steady-state profiles do not depend on the initial arrangement. This independence has been verified by comparing with simulations with the same small-particle fraction $\overline{\phi^s}$ in which the large particles are initially lying on top of the small particles. The total mass of flowing grains per unit planar area is fixed across all simulations to $60\rho_*d^s$, resulting in a flow height $h \approx 100d^s$. A complete list of all DEM simulations on an inclined plane performed in this paper is provided in [Appendix A](#).

2.2. Segregation behaviour

Mixtures of size ratio $R = 3$ segregate in a conventional way with large particles rising to the surface ([figure 1a](#)). However mixtures with $R = 6$ exhibit a new and qualitatively

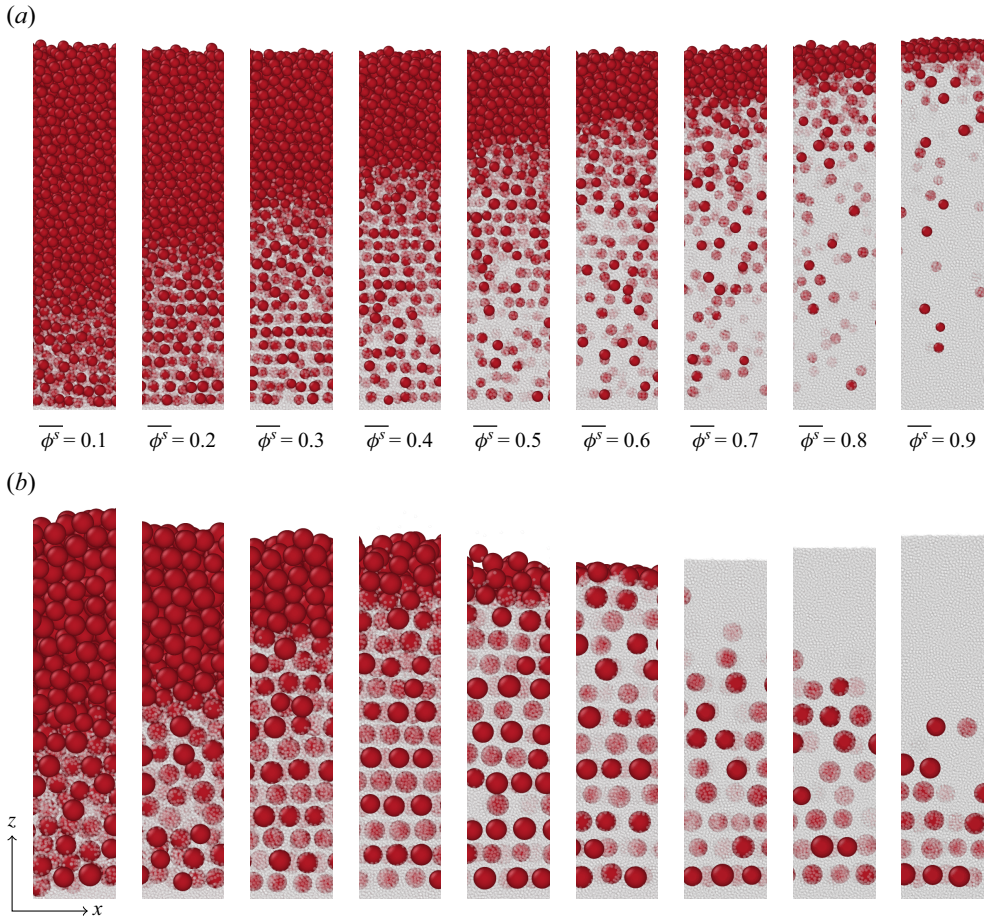


Figure 1. Snapshots of 18 bidisperse DEM simulations in steady state on a plane inclined at 25° . The small (white) particles are rendered partially transparent to improve the visibility of the large (red) particles. Shown are flows at size ratios (a) $R = 3$ and (b) $R = 6$. In both rows, the small-particle fraction $\bar{\phi}^s$ increases from $\bar{\phi}^s = 0.1$ to $\bar{\phi}^s = 0.9$ in each plot from left to right. At $R = 3$ the large particles always rise and accumulate at the surface, irrespective of $\bar{\phi}^s$. The behaviour at $R = 6$ is qualitatively different, with either large or small particles accumulating at the surface, depending on $\bar{\phi}^s$.

different segregation behaviour (figure 1b) in which large particles may either rise or sink, or where segregation is strongly suppressed and the grains are almost uniformly mixed throughout the flow depth. The large particles may also form distinct layers which are separated by thin bands of small particles.

At $R = 6$, whether large or small particles accumulate at the surface depends on the small-particle fraction $\bar{\phi}^s$. For $\bar{\phi}^s \gtrsim 0.7$, the large particles are concentrated near the base of the flow (figure 1b), while their concentration decreases towards the surface. A surface layer of purely small particles forms, rendering the large particles invisible when viewed from above. For lower $\bar{\phi}^s \lesssim 0.5$ the segregation behaviour changes as the large particles accumulate at the surface, forming a pure layer devoid of small particles. The transition between these regimes occurs at $\bar{\phi}^s \approx 0.6$, where the distribution of particles is almost uniform with depth.

This behaviour differs markedly from the well-described behaviour at $R = 3$ where the large particles segregate to the surface at all values of $\bar{\phi}^s$, while their concentration

decreases with depth (figure 1*a*). The rise of large particles (of equal intrinsic density) is typical of segregation in bidisperse mixtures of size ratio three or less (Savage & Lun 1988; Golick & Daniels 2009; Wiederseiner *et al.* 2011; van der Vaart *et al.* 2015). In contrast to the segregation behaviour of grains of only slightly varying size, at size ratio $R = 3$ the uppermost part of the flow is composed solely of large particles, with the small particles totally absent. The thickness of this layer decreases as the fraction of small particles $\bar{\phi}^s$ increases.

The phenomenon of large particles sinking when present in low concentrations and settling close to the base of the flow was termed reverse segregation by Thomas (2000), who observed this behaviour in deep chute flows of small particles with a small proportion of large grains added ($\bar{\phi}^s \geq 0.9$). The simulations performed in this paper at $R = 6$ show that as the fraction of large particles in the flow is increased (i.e. as $\bar{\phi}^s$ is decreased), the large particles progressively fill upwards from the base (figure 1*b*). At $\bar{\phi}^s = 0.6$ the large particles reach the surface and there is an approximately uniform distribution throughout the depth. For $\bar{\phi}^s < 0.6$, there are sufficient large particles that they form a pure layer on the surface, riding on top of a mixed region of small and large particles in a configuration that is more similar to segregation at $R = 3$.

Notably, the small-on-top case at $R = 6$ ($\bar{\phi}^s \gtrsim 0.7$) is qualitatively different from simply flipping the corresponding large-on-top case at $R = 3$ upside down. In particular, at $R = 6$ the large particles do not form a pure basal layer, but remain intermixed with small particles near the base (figure 1*b*). Furthermore, in these mixed small- and large-particle regions, large particles are organised into discrete horizontal layers, with each layer being one large particle thick. These layers are separated by thin regions of small particles, and adjacent large particles do not appear to make direct contact. This layering of large particles is discussed in detail in § 3.

The segregation patterns in the images of figure 1 can be represented in continuum concentration profiles, where the concentration ϕ^ν is defined as the local volume fraction of species ν per unit granular volume, where $\nu = s, l$ for small and large particles, respectively. Continuum concentration fields are constructed using the coarse-graining method of Tunuguntla *et al.* (2016) with a Gaussian smoothing function as described in Appendix B. The coarse-graining width is set to $c = 0.8d^l$, a value chosen from a plateau on which continuum fields are insensitive to the coarse-graining width (Tunuguntla *et al.* 2016). Choosing this coarse-graining width comparable to the large-particle diameter suppresses oscillations that would occur at smaller coarse-graining widths, due to the particle-scale layering observed in figure 1. This allows the underlying variation in bulk composition to be studied.

Figure 2 shows such continuum volume fraction profiles $\phi^s(z)$ for the simulations illustrated in figure 1. At $R = 3$ (figure 2*a*) the small-particle concentration ϕ^s decreases with height over all small-particle fractions, indicating segregation in which the large particles accumulate at the surface. By contrast, at $R = 6$ (figure 2*b*) there is a distinct switch in behaviour of the profiles when the local concentration ϕ^s reaches a specific ‘neutral’ value $\phi_n^s \approx 0.6$ (dashed line in figure 2*b*), which separates the large-on-top and small-on-top configurations. For $\phi^s < \phi_n^s$, the profiles decrease with height resulting in a large-particle layer at the surface. For $\phi^s > \phi_n^s$, the concentration profiles increase with height resulting in a small-particle surface layer. Near the neutral concentration $\phi^s \approx \phi_n^s$, the mixture is at an almost uniform concentration with depth. The local concentration ϕ^s therefore plays a crucial role in determining whether large particles sink towards the base, rise to the surface or remain at the same depth.

The influence of the size ratio R on segregation is illustrated in figure 3. At fixed $\bar{\phi}^s = 0.7$, increasing R from 2 progressively reduces the thickness of the surface layer of large

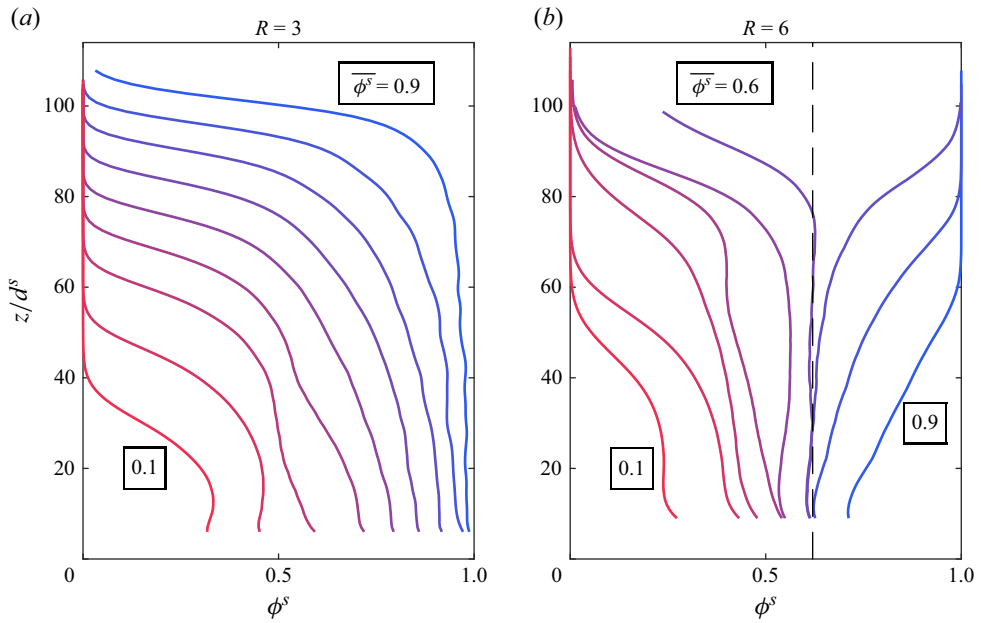


Figure 2. Profiles of small-particle concentration ϕ^s as a function of slope-normal coordinate z for (a) $R = 3$ and (b) $R = 6$. Coloured lines represent different small-particle fractions, $\bar{\phi}^s$, increasing from 0.1 (red) to 0.9 (blue) in increments of 0.1. Selected values of $\bar{\phi}^s$ are indicated on the plots. In (b), the dashed line at $\phi^s = 0.62$ separates simulations with a surface composed of small particles and those with a large-particle surface.

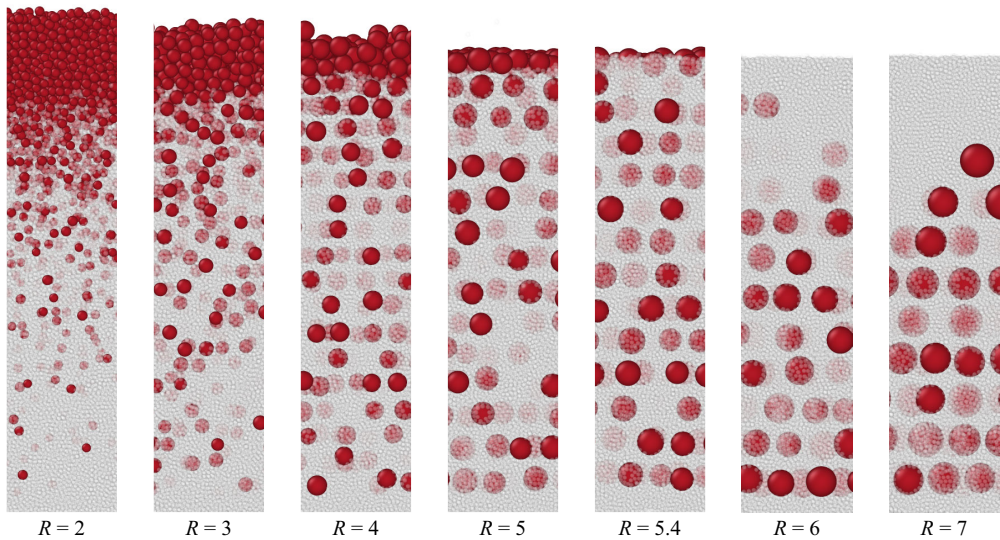


Figure 3. Snapshots of bidisperse DEM simulations in steady state on a plane inclined at 25° , with the flow going from left to right within each panel. The small (white) particles are partially transparent to improve the visibility of the large (red) particles. The small-particle fraction is fixed at $\bar{\phi}^s = 0.7$, and the size ratio increases from $R = 2$ to $R = 7$ as indicated beneath the images.

particles. At $R = 5$ this layer is only one large particle thick and the mixture becomes nearly uniform with depth, similar to the behaviour observed for $R = 6$ at $\bar{\phi}^s = 0.6$. At $R = 5.4$, there is no longer a distinct surface layer of large particles, with both small and large particles lying at the surface and a near-homogeneous mixture throughout the depth. As R is increased further (to 6 and 7) the large particles are concentrated towards the flow base, and are entirely absent from the surface.

We hypothesise that the transition from a small-particle surface to a large-particle surface, as the fraction of large particles increases, arises from a competition between two mechanisms: the effective density effect discussed in the introduction and the migration of small particles through voids. At low concentrations of large particles, their higher density relative to the surrounding medium of small particles and void space causes them to sink. This displaces the smaller particles upward, and results in a surface layer composed of entirely small particles. As the concentration of large particles increases, the large particles are no longer isolated but are in close proximity to other large particles, and the average density of the granular mixture surrounding a large particle rises, decreasing the density difference. Once the large particles are densely packed, the mechanisms of kinetic sieving and squeeze expulsion may take place, allowing small particles to fall downwards through the voids between large particles, displacing them upward. At sufficiently high fractions of large particles, this process leads to a layer of large particles at the surface above a mixed region of large and small particles.

2.3. Neutral concentration

Whether the free surface of an inclined-plane flow is made up of small or large particles (that is, whether large particles have a tendency to sink or rise, respectively) depends on both the size ratio R and the small-particle fraction $\bar{\phi}^s$. At $R = 6$ the transition occurs close to $\bar{\phi}^s \approx 0.6$ (figure 2*b*), while at $R = 5.4$ it shifts to $\bar{\phi}^s \approx 0.7$ (figure 3). Close to the transition, the concentration profiles are approximately uniform with depth. Simulations can therefore be grouped into those with a large-particle surface and those with a small-particle surface, as shown in figure 4. A simulation is defined to have a large-particle surface if its $\phi^s(z)$ profile moves towards $\phi^s = 0$ as $z \rightarrow h$, as seen for all cases with $\bar{\phi}^s \leq 0.6$ in figure 2*b*), for example. At a given R , the transitional value of $\bar{\phi}^s$ corresponds to the value of the local concentration ϕ^s at which the profiles become approximately uniform with depth. This is the neutral concentration ϕ_n^s . Therefore the black line sketched in figure 4, which approximately separates flows with a large- and small-particle surface, is the curve $\bar{\phi}^s = \phi_n^s(R)$.

These results connect to the more well-studied limit of a single large intruder. Our DEM simulations on an inclined plane with a single large intruder within a flow of small grains show that the intruder remains at or just below the surface for $R \leq 3.8$ and sinks towards the base for $R \geq 4$; this is consistent with previous studies (Thomas & D'Ortona 2018; Jing *et al.* 2020). In figure 4, these single-intruder simulations appear with $\bar{\phi}^s = 1$, since the flow is made up of entirely small particles apart from a single large grain. Therefore the value of R for which $\phi_n^s \approx 1$ is approximately $R \approx 4$.

3. Layering

In many of the DEM simulations, in regions of mixed large and small particles, the large particles form distinct horizontal layers (visible in figures 1 and 3, particularly for larger size ratios $R \gtrsim 4$). The layered structure is striking and marks a key distinction between segregation at large size ratios and that at lower size ratios ($R < 3$), where such layering is not observed. The primary objective of this section is to determine whether such layering is

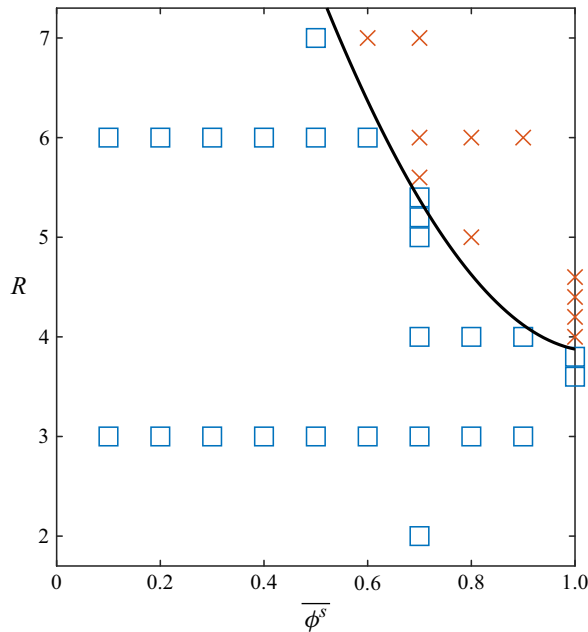


Figure 4. Size ratio R and small-particle fraction $\bar{\phi}^s$ for which mixtures have a small- or a large-particle surface at $\theta = 25^\circ$. Blue squares indicate a large-particle surface and orange crosses indicate a small-particle surface. The sketched black curve divides the two regimes and represents the neutral concentration $\phi_n^s(R)$.

intrinsic to real, size-bidisperse granular flows, rather than an artefact arising from periodic boundary conditions, a relatively small system size in simulations or proximity to the flow base/surface in shallow flows in chutes and on inclined planes. To investigate this, inclined-plane and Lees–Edwards DEM simulations are performed, alongside laboratory experiments in a rectangular chute.

3.1. Inclined-plane simulations

In the inclined-plane simulations, the initial configuration consists of smaller particles above the larger ones. Once flow commences, the small particles begin to filter down towards the base, but no layering is apparent after a short time, as shown in [figure 5\(a\)](#) for $R = 6$ and $\bar{\phi}^s = 0.4$ at $t = 120(d^s/g)^{1/2}$. With continued flow, however, the system transitions into a layered structure as shown in [figure 5\(b\)](#). A video of the transition into a layered state is available in supplementary movie 1 available at <https://doi.org/10.1017/jfm.2026>.

The overall layered and segregated structure is recovered after $t \approx 600(d^s/g)^{1/2}$ as shown in [figure 5\(c\)](#), in which the small-particle concentration ϕ^s is plotted as a function of z and t . For context, with typical small grain size $d^s = 100 \mu\text{m}$, a flow depth $h = 1 \text{ cm}$ and gravitational acceleration $g = 9.8 \text{ m s}^{-2}$, this corresponds to a time $t \approx 1.9 \text{ s}$. To resolve the layers, the simulations are coarse-grained with a width of $c = 0.2d^s$, as indicated by the notation $\phi^s(t, z; c = 0.2d^s)$ ([Appendix B](#)). This very small coarse-graining width effectively visualises the vertical distribution of large-particle centres, rather than the volume occupied by the large particles. The width of the red stripes is indicative of the variation in the z position of large-particle centres within a layer, typically $\lesssim 0.4d^l$ in the lower half of the flow in [figure 5\(b,c\)](#), and increasing towards the surface.

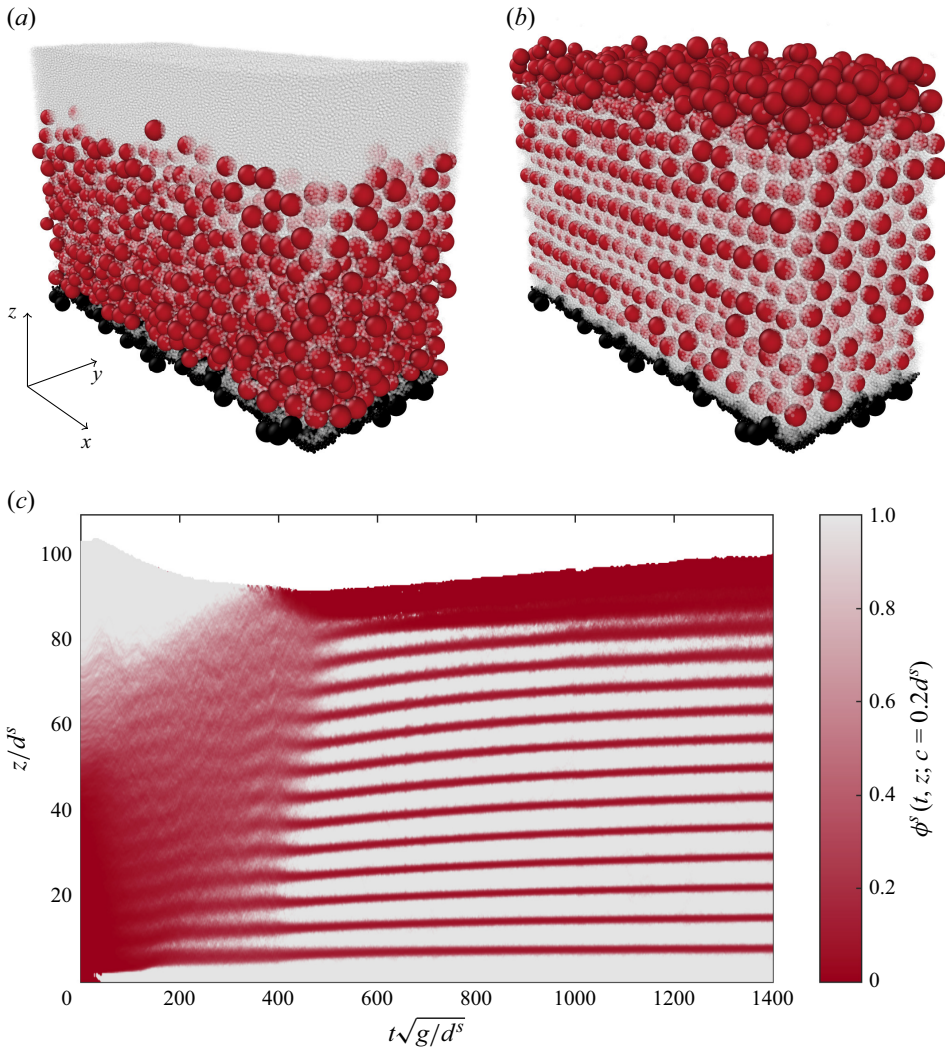


Figure 5. A bidisperse DEM simulation at size ratio $R = 6$ and small-particle fraction $\bar{\phi}^s = 0.4$ on a plane inclined at 25° . Snapshots (a) at $t = 120(d^s/g)^{1/2}$, after flow and segregation have commenced but before layering has occurred, and (b) at $t = 1000(d^s/g)^{1/2}$, in a layered state. The small (white) particles are partially transparent to improve the visibility of the large (red) particles. Flow is in the positive x direction. (c) The time evolution of the small-particle concentration ϕ^s along the slope-normal direction z , using a coarse-graining width of $c = 0.2d^s$ to resolve the layers. The full transition into the layered state is shown in supplementary movie 1.

Successive layers form in the direction of the velocity gradient (i.e. along the z axis), with each layer lying in the x - y plane. The lowest layer forms approximately three small particle diameters above the base, and the layered structure extends upward through the flow. The layers are one large particle thick, with large particles separated by thinner regions of small particles typically one to three small-particle diameters thick. The separation between layers, measured as the distance between large-particle centres in adjacent layers, is approximately constant and is equal to $d^s + d^l$, although this distance increases slightly as the flow dilates (figure 5c). This layered arrangement extends upward

until either the number of large particles becomes insufficient to sustain additional layers or the flow transitions into a nearly monodisperse region of large particles near the surface. In the latter case, the lack of small particles prevents them from effectively separating the large-particle layers, causing the layered structure to break down. Thus, the layering here is present in bidisperse regions but disappears when the flow is approximately monodisperse, indicating a qualitatively distinct mechanism from the crystallisation that can occur in monodisperse flows (Silbert *et al.* 2002). Layers are less distinct in simulations with low small-particle fractions (e.g. $\overline{\phi^s} = 0.1$ and 0.2 in figure 1*b*), again pointing to a lack of small particles inhibiting layer formation.

Layering may be identified from the small-particle concentration ϕ^s profiles, computed using a fine coarse-graining width $c = 0.2d^s$. The ϕ^s fields are averaged in the flow (x) and cross-flow (y) directions, so only the variation in the velocity-gradient (z) direction, in which the layers form, remains. In these profiles, layers appear as sequence of alternating maxima and minima (figure 5*c*). A minimum is classified as a large-particle layer if two criteria are satisfied: (i) the amplitude between the minimum and both its adjacent maxima exceeds 0.3 and (ii) the vertical separation between successive minima is $d^l \leq \Delta z \leq 1.5d^l$. The small-particle concentration ϕ^s associated with this layer is estimated by coarse-graining the profile at that height using a broader width $c = 0.8d^l$, which smooths over the oscillations. The coarse-graining procedure is described in Appendix B.

Layering does not occur across all size ratios R or local small-particle concentrations ϕ^s . Rather, applying the above definition of layering to all of the simulations in figure 2(*b*) indicates that, for $R = 6$, layering emerges within the range $0.28 \lesssim \phi^s \lesssim 0.86$. Below this range, the proportion of large particles is too high for distinct layers to form. At very high ϕ^s there are too few large particles to distinguish layers.

Some layering is also present at $R = 3$, particularly for the simulations at $\overline{\phi^s} = 0.3$ and 0.4 (figure 1*a*). However the layering appears over a narrower range of concentrations, approximately $0.32 \lesssim \phi^s \lesssim 0.76$ at this size ratio. Furthermore, the layers at $R = 3$ are less distinct than at $R = 6$, suggesting that layering becomes more pronounced and appears over a wider range of ϕ^s as the size ratio increases. Supporting this trend, the set of simulations at $\overline{\phi^s} = 0.7$ in figure 3 display clear layering for $4 \leq R \leq 7$ but not for the smaller size ratios $R = 2$ and 3 .

The profiles of the down-slope velocity u in figure 6(*a*) and corresponding small-particle concentration ϕ^s profiles in figure 6(*b–d*), which are taken from figure 5(*c*) at the times indicated, reveal a feedback of layering on the flow rheology. After layering occurs, the velocity profiles acquire a stepped structure, with each step corresponding to one layer, while becoming increasingly linear across the entire layered region. By $t = 1400(d^s/g)^{1/2}$ the shear rate begins to decrease only in the thin, approximately monodisperse, region of large particles near the flow surface. This near-linear profile may suggest the rheology in layered bidisperse mixtures deviates from the Bagnold scaling (Bagnold 1954) and, consequently, from constitutive relations based on the $\mu(I)$ rheology (Jop, Forterre & Pouliquen 2005; Rognon *et al.* 2007; Tripathi & Khakhar 2011).

As layering develops, the flow near the free surface accelerates, an effect that is visible in figure 6(*a*) and in supplementary movie 1. In contrast, the flow near the base becomes slower. The flow also dilates after layering occurs as figure 6(*c,d*) shows, with individual layers rising upwards, even though most segregation is already complete. These behaviours are consistent with a feedback between layering and rheology. Figure 6 suggests that the relationship between layering and rheology is rich and potentially complex. A detailed characterisation lies beyond the scope of this paper.

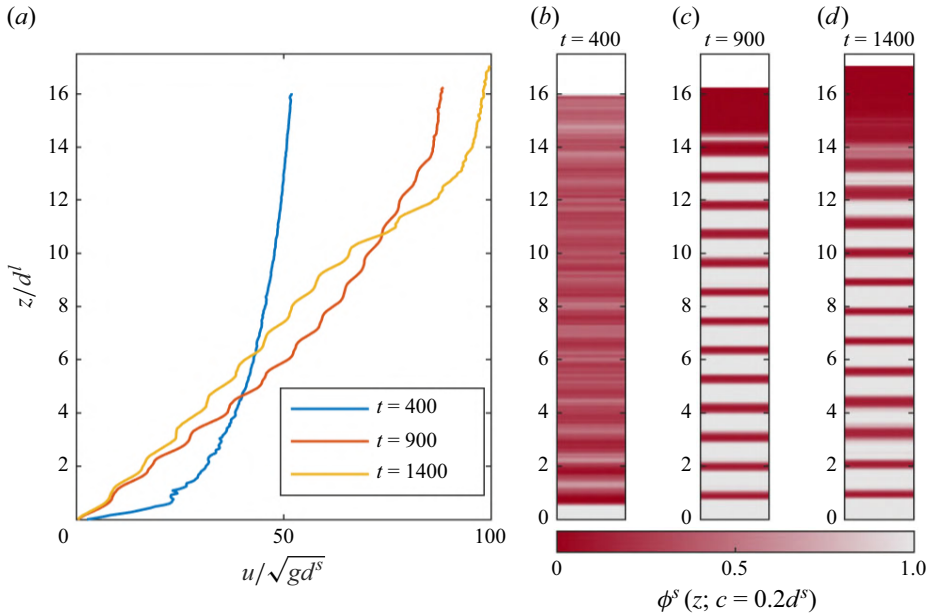


Figure 6. (a) The down-slope velocity profiles $u(z)$ plotted against the slope-normal coordinate z at times before and after layering occurs, for the bidisperse inclined-plane flow at $R=6$ in figure 5. The times are given in units of $(d^s/g)^{1/2}$. The corresponding small-particle concentration ϕ^s profiles at times (b) $t=400$, (c) $t=900$ and (d) $t=1400$. Note that the vertical scale is z/d^l . All profiles are from the simulation in figure 5 and computed with a coarse-graining width $c=0.2d^s$.

3.2. Lees–Edwards simulations

In the inclined-plane simulations, grains are subject to a gravitational body force, which drives segregation. Furthermore there is a rigid rough boundary at $z=0$. To test whether either gravity or the presence of a boundary is necessary for layering, DEM simulations are performed in LAMMPS (Thompson *et al.* 2022) with Lees–Edwards boundary conditions (Lees & Edwards 1972). These boundary conditions impose a simple shear velocity profile $\mathbf{u} = (\dot{\gamma}z, 0, 0)$ with shear rate $\dot{\gamma}$ and are implemented in LAMMPS via the `fix deform` command which shears the simulation domain and is equivalent to the standard sliding brick representation (Evans & Morriss 2007). These simulations are performed in a fully periodic, three-dimensional domain with no rigid boundaries. Gravity is absent and so gravity-driven segregation does not occur.

A bidisperse mixture is simulated at a size ratio $R=6$, a small-particle concentration $\phi^s=0.5$ and total solids volume fraction $\Phi=0.63$, a value representative of the simulations on an inclined plane at $R=6$. A polydispersity of 10% either side of the mean diameter d^s is retained for the small particles, whilst the large particles are strictly monodisperse with diameter d^l . In these simulations the large particles are given a single diameter to more clearly study the separation between them, though introducing $\pm 10\%$ polydispersity among the large particles does not qualitatively change the behaviour seen. A fixed binary collision time of $t_c=0.00125/\dot{\gamma}$ is used, ensuring the particles are in the asymptotic hard-particle regime where the rheology is independent of the particle stiffness (Chialvo, Sun & Sundaresan 2013). Other particle interaction parameters are the same as those described in § 2.1. Similarly to the inclined-plane simulations, a Cartesian coordinate system is chosen with x representing the flow direction, y the vorticity direction and z the velocity-gradient direction. The box lengths are $L_x=48d^l$, $L_y=10d^l$ and $L_z=12d^l$ in

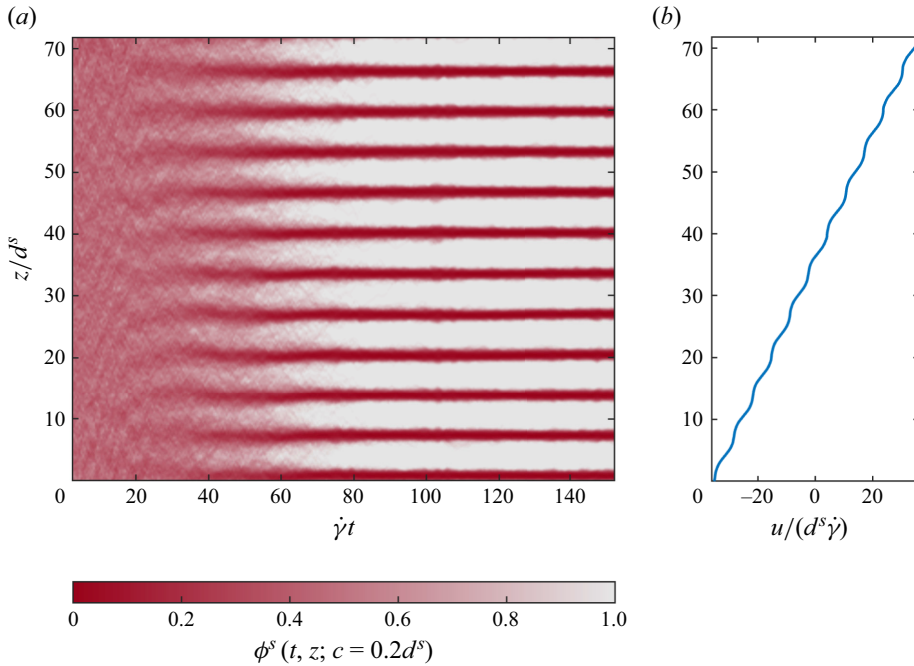


Figure 7. The time-dependent formation of layers in a Lees–Edwards simulation at $R = 6$. The system is periodic in all spatial directions and so is invariant to a shift in the z axis. (a) The small-particle concentration ϕ^s as a function of velocity-gradient coordinate z and time t . To resolve the layered structure, a coarse-graining width $c = 0.2d^s$ is used. The transition into a layered structure is shown in supplementary movie 2. (b) The corresponding velocity profile at $\dot{\gamma}t = 132$.

the x , y and z directions, respectively. These lengths are varied to ensure the conclusions are independent of domain size. Particles are initially placed at random positions within the domain.

Despite starting in a random, unlayered configuration, once a shear velocity profile has been imposed, the grains transition into a layered state as shown in figure 7, which plots the small-particle concentration as a function of time t and velocity-gradient coordinate z , with a coarse-graining width $c = 0.2d^s$. The layered structure is qualitatively similar to that in inclined-plane simulations (figure 5c), with the layers emerging from a disordered state and forming along the velocity-gradient direction. Successive layers are again separated by regions of small particles. The evolution into a layered state is shown in supplementary movie 2. Lees–Edwards boundary conditions impose a linear velocity profile, which remains even after layering has occurred; however, the velocity profile becomes stepped around the overall linear variation (figure 7b). Each step corresponds to a single large-particle layer, consistent with figure 6(a).

By $\dot{\gamma}t = 60$, the system has evolved into a clearly layered state (figure 7). All Lees–Edwards simulations performed exhibited layering by this time, but the time scale depended somewhat on the streamwise box length L_x . Larger boxes generally layered more slowly, but this dependence plateaued for $L_x \geq 48d^l$. For reference, two large particles separated by a distance d^l in the z direction would take a non-dimensional time $\dot{\gamma}t = L_x/d^l$ to shear apart from one another by the streamwise box size L_x and approach each other again due to the periodic boundaries. In the largest domains studied ($L_x = 200d^l$), this time is $\dot{\gamma}t = 200$, well above the observed layering time of $\dot{\gamma}t \approx 60$. Hence, layering

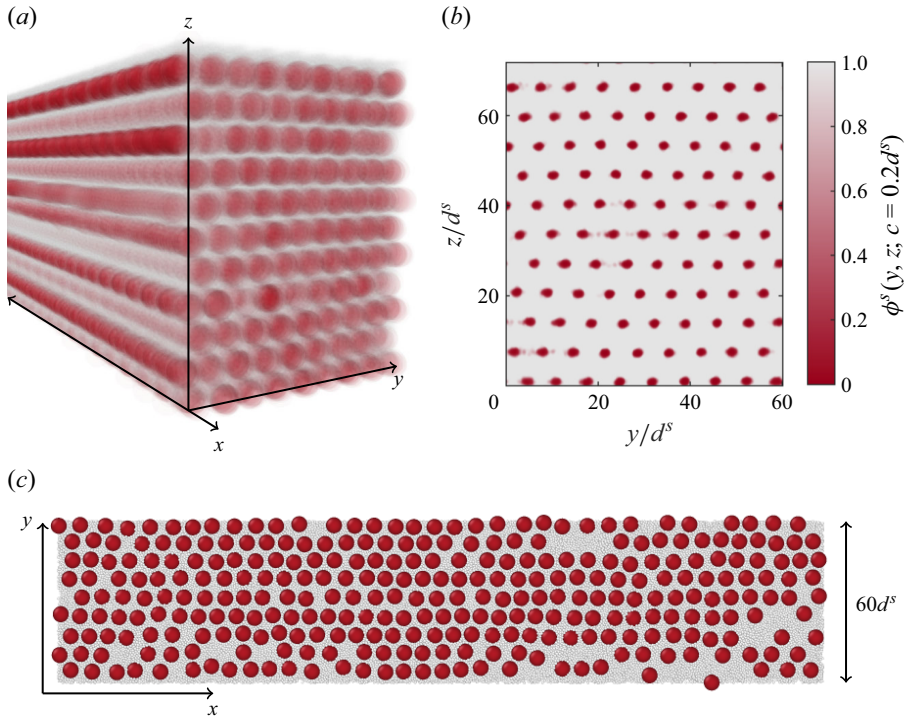


Figure 8. Layered structure in a Lees–Edwards simulation at $R = 6$. (a) A snapshot of the layering, obtained by averaging 50 frames over a time interval $25/\dot{\gamma}$. Flow is in the positive x direction. (b) The small-particle concentration as a function of the velocity-gradient coordinate z and cross-flow coordinate y . A coarse-graining width $c = 0.2d^s$ is used to resolve the layered structure. (c) The structure in the x – y plane, of the lowest layer in (a,b).

occurs on a time scale shorter than that required for such periodic boundary effects. The layering time showed little sensitivity to the box dimensions in the y and z directions.

Within each layer of large particles, large particles are arranged into straight lines parallel to the flow direction (figure 8). These chains of large particles can be seen in the image in figure 8(a), which is obtained by averaging 50 frames over a time interval of $25/\dot{\gamma}$ once the simulation has layered. Chains are also present in the inclined-plane simulations as shown in figure 5(b) and supplementary movie 1. Each large particle tends to follow directly behind the one ahead, creating extended chains that can span the entire periodic domain, even for the longest streamwise box length of $200d^l$ tested in this study.

The chains of large particles are further illustrated in figure 8(b) which plots the small-particle concentration ϕ^s as a function of cross-flow coordinate y and velocity-gradient coordinate z , averaged over the box length $48d^l$ in the streamwise direction. The small-particle concentration ϕ^s from the simulation in figure 8(a) is used, with a coarse-graining width of $c = 0.2d^s$. Each red dot therefore represents a large-particle chain. The chains are regularly spaced in the y direction and, combined with the layering in the z direction, they produce the hexagonal pattern visible in figure 8(b). With the box size chosen this arrangement does not form a perfectly regular lattice. The box, of length $12d^l$ in the z axis, results in 11 layers, making the periodicity inconsistent with a regular lattice. Despite this constraint, a lattice-like structure still emerges. A similar, though weaker, hexagonal arrangement is also observed in the x – y structure of a single layer, shown in figure 8(c), which corresponds to the lowest layer (closest to $z = 0$) in figure 8(a,b).

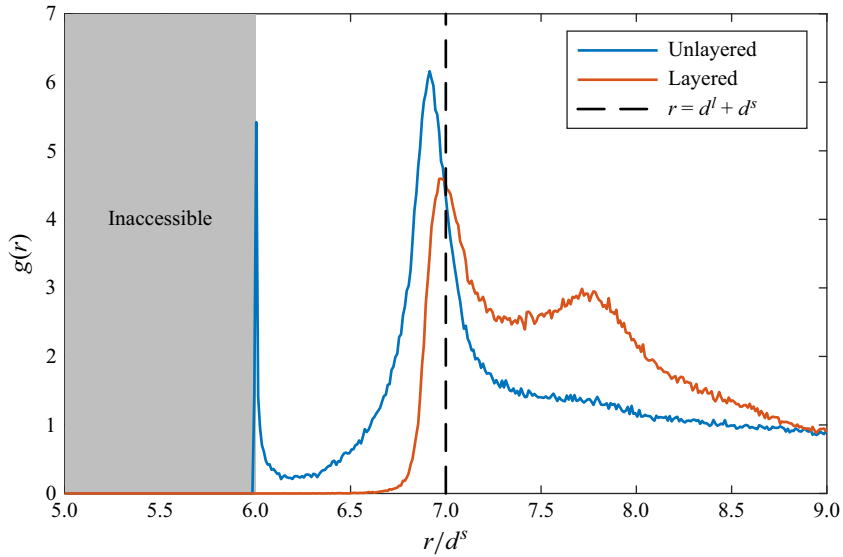


Figure 9. The RDF $g(r)$ for large-particle pairs at $R = 6$, as defined in (3.1), with bin width $\Delta r = 0.01d^s$. The blue line represents an unlayered state measured at time $\dot{\gamma}t = 22$ and the red line a layered state measured at $\dot{\gamma}t = 132$. The shaded region indicates $r < d^l = 6d^s$, where large-particle centres cannot lie due to volume exclusion. The dashed vertical line marks the distance $r = d^l + d^s = 7d^s$, corresponding to large particles separated by one mean small-particle diameter.

The self-organisation of large particles into a regular structure (figure 8), with layers forming in the z direction and chains extending in the x direction, indicates that the large particles arrange themselves in a way that minimises collisions between neighbouring large particles. The avoidance of direct contact between large particles is evidenced by the radial distribution function (RDF), $g(r)$, for large-particle pairs (figure 9). The RDF provides a measure of the probability of finding a large-particle centre at distance r from the centre of a reference large particle, relative to the probability expected for a uniform distribution at the same number density. Peaks and troughs in $g(r)$ indicate preferred separations or avoidance, while, in a homogeneous system, $g(r)$ approaches 1 in the asymptotic limit $r \rightarrow \infty$, indicating particle positions are uncorrelated at large distances. Specifically, the RDF is defined as (Wiacek 2016)

$$g(r) = \frac{N(r)}{n^l 4\pi r^2 \Delta r}, \quad (3.1)$$

where n^l is the number density of large particles and $N(r)$ is the number of large particles with centres in a spherical shell of thickness Δr , located at radial distance r from the centre of a reference particle. In this study $\Delta r = 0.01d^s$ is used. Time-averaging is performed on $g(r)$ using 29 evenly spaced snapshots over a time interval of $14/\dot{\gamma}$.

There is a striking difference between the RDFs before and after layering occurs (figure 9). At $R = 6$, in an unlayered state, $g(r)$ exhibits a peak around $d^l + d^s = 7d^s$ indicating that, with these simulation parameters, large particles preferentially position themselves around one mean small-particle diameter apart. There is a second, sharper peak at $r = 6d^s = d^l$, representing large particles in direct contact. This peak is likely sharper because the large particles here have no polydispersity: when they are in direct contact, their centres are separated by exactly d^l . Values $r < d^l$ are not permissible due to volume exclusion, apart from some small overlaps allowed by the soft-sphere DEM. In contrast,

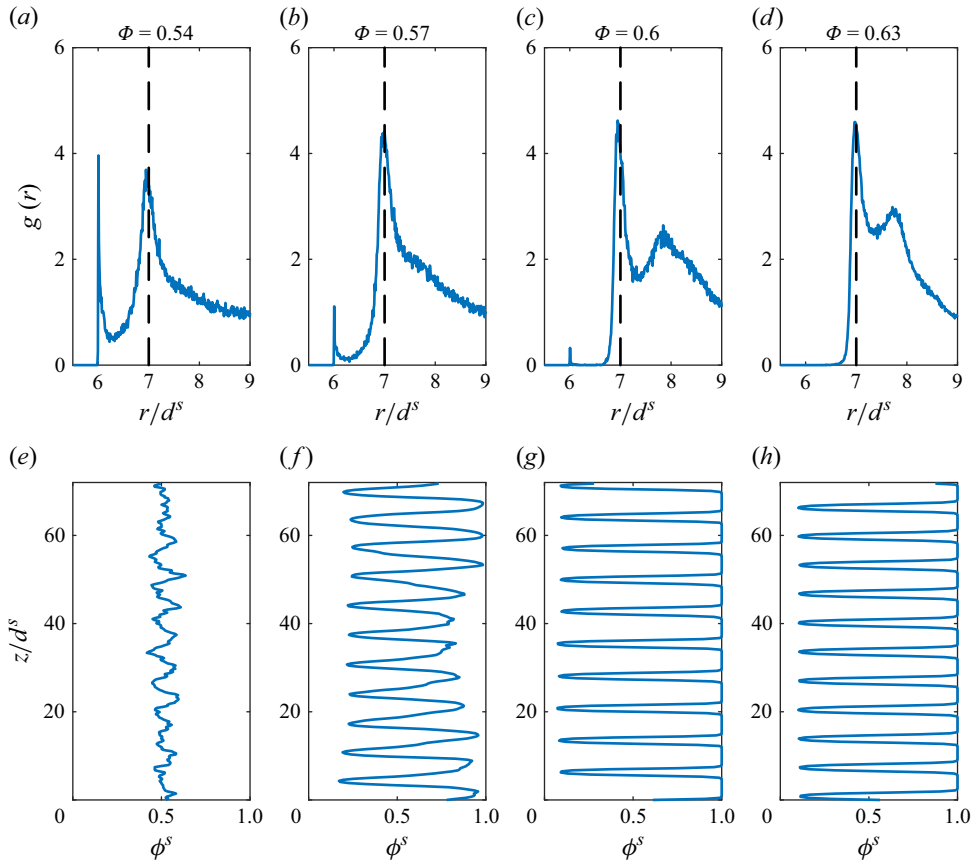


Figure 10. The RDFs $g(r)$ for large-particle pairs from Lees–Edwards simulations at size ratio $R = 6$, small-particle concentration $\phi^s = 0.5$ and solids volume fraction Φ of (a) 0.54, (b) 0.57, (c) 0.6 and (d) 0.63. The dashed vertical line marks the distance $r = d^l + d^s = 7d^s$, corresponding to large particles separated by one mean small-particle diameter. (e–h) The corresponding vertical ϕ^s profiles, coarse-grained at $c = 0.2d^s$, directly beneath their associated RDFs. The system is periodic in all spatial directions and so is invariant to a shift in the z axis.

once layering has occurred, the peak at $r = d^l$ vanishes, and $g(r = d^l) \approx 0$, indicating that large particles no longer make direct contact. In fact, $g(r) < 0.1$ for $r < 6.7d^s$ showing that large particles rarely approach each other at separations much smaller than one small-particle diameter. Instead, they are kept apart by thin regions of small particles, evidenced by the peak in simulation at $r \approx d^l + d^s$ showing that the large particles are positioned approximately one small particle away from their nearest neighbour in this simulation. Qualitatively similar behaviour is observed for mixtures with different ϕ^s once layering develops.

The structure of bidisperse flows depends on the solids volume fraction Φ , as evidenced by the differences in the RDFs for $0.54 \leq \Phi \leq 0.63$ (figure 10a–d). All RDFs are computed at size ratio $R = 6$ and small-particle concentration $\phi^s = 0.5$. At the lowest solids volume fraction of $\Phi = 0.54$, there is a pronounced peak at $r = d^l$, indicating large particles in direct contact. As Φ increases, this peak diminishes then disappears as the large particles are separated by thin bands of small particles. For reference, the jamming fraction at $R = 6$ and $\phi^s = 0.5$ is approximately 0.7 (Srivastava *et al.* 2021), so all cases considered are well below jamming and are outside of the quasi-static regime.

The changes in the RDFs are reflected in the $\phi^s(z)$ profiles when coarse-grained with $c = 0.2d^s$ (figure 10*e–h*). At $\Phi = 0.54$, the flow is largely disordered and layering does not occur, allowing large particles to make direct contact, although there is some indication of a weak periodic structure. As Φ increases to 0.57, 0.6 and 0.63, clear layering occurs, with large particles organised into increasingly well-defined bands. These observations indicate that layering not only depends on R and ϕ^s , but also on the solids volume fraction Φ , with layering less likely in more dilute flows. Consequently, the phase space governing layering is at least three-dimensional, depending on R , ϕ^s and Φ .

The emergence of the layered structure in a gravity-free, fully periodic shear cell suggests that large-particle layering is caused only by shear. In particular, it implies that neither gravity nor a rigid boundary are necessary for layering, although the presence of a rigid base may promote particle ordering (Weinhart *et al.* 2013). Shear-driven ordering has recently been seen in simulations of dense, frictional size-bidisperse suspensions at a size ratio of three (Malbranche, Chakraborty & Morris 2023), where the large particles arranged themselves into distinct layers separated by thin regions of small particles. This behaviour is qualitatively similar to that seen in figure 8 and supplementary movie 2 and suggests that layering is a generic behaviour of size-bidisperse particle mixtures, rather than being due to the particular dry granular friction behaviour considered in this paper. The alignment of large particles into chains is also consistent with the experimental and numerical study of Fraysse *et al.* (2024), who showed that two large intruders in an inclined-plane flow of otherwise monodisperse small particles tend to align with the flow, over a range of flow depths and slope angles. The results in this paper indicate that this alignment is robust and extends to many large particles.

3.3. Experiments

To experimentally validate the layer formation present in DEM simulations, an experimental configuration was chosen that subjects a deep region of size-bidisperse grains to sustained simple shear flow. The set-up consists of an enclosed rectangular chute, inclined steeply at $\theta = 70^\circ$ to the horizontal, with a gate restricting the outflow flux (figure 11). This configuration creates a region of shearing flow at least 16 large particles (≈ 100 small particles) deep. The experiment provides a means to test whether large-particle layering occurs outside the constraints of periodic simulation domains. To our knowledge, the formation of large-particle layers similar to those in figure 5(*b*) has not previously been observed in real granular flows.

The top and bottom boundaries of the experiment are 53 mm apart, and are roughened to induce shear using 40 grit aluminium oxide paper. The transparent front and back walls are separated by 18 mm and allow direct visualisation of the flow. The chute is 120 cm long and a camera films a portion of the flow, 16 cm from the outflow. A bidisperse mixture of dry spherical glass beads is used, consisting of small white (diameter 200–300 μm) and large red (diameter 1.40–1.65 mm) grains, with a mean size ratio $R \approx 6$. The intrinsic density of the small and large beads is 1440 and 1510 kg m^{-3} , respectively. The chute is filled with 0.7 kg of small grains and 0.5 kg of large grains, which are initially approximately uniformly mixed. The formation of layers is robust and not sensitive to the precise initial conditions. Material exits the chute through a gate at the bottom which pivots around a point at the base of the right-hand boundary, as indicated in figure 11, to create a partial opening for the grains to flow through. The grains land on a balance that records the mass as a function of time. A video of the full experiment is available in supplementary movie 3.

The mass flux exiting the chute quickly stabilises at a steady value of 0.07 kg s^{-1} approximately 1 s after the gate is opened. Within the shearing region, the initially

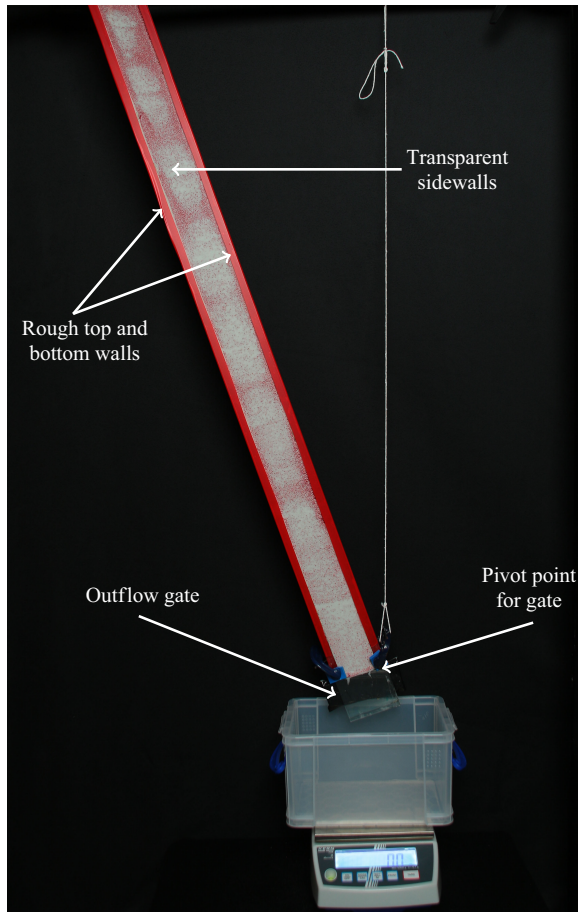


Figure 11. Experimental set-up for the rectangular chute prior to the release of the grains. The chute is inclined at 70° to the horizontal and is 120 cm long, with transparent, glass sidewalls spaced 18 mm apart. The top and bottom boundaries are roughened with 40 grit aluminium oxide paper and are separated by 53 mm. At the lower end, grains are held in place by a gate that pivots at the right-hand boundary. When opened, the gate creates an opening at the bottom boundary, allowing particles to exit. The grains fall onto a mass balance that records mass as a function of time. In steady state, the measured mass flux is 0.07 kg s^{-1} . The full experiment is shown in supplementary movie 3.

disordered state (figure 12a) evolves into an ordered, layered structure (figure 12b). The full transition into the layered state can be seen in supplementary movie 4, and a slow-motion version is available in supplementary movie 5. Layering emerges rapidly once the flow is underway, with visible evidence that large particles have formed layers apparent around 2 s after the gate has opened. The layering persists until the chute is fully emptied, at approximately 17 s.

The layering of grains occurs primarily where significant shear is present in the flow, as evidenced by the velocity profile sketched in figure 12(b). This profile, which is based on the tracked deformation of 13 large particles, illustrates the deformation of an initially straight line element, oriented normal to the slope. The shear rate is reduced near the base due to lateral confinement by the sidewalls (Jop, Forterre & Pouliquen 2006; Lloyd *et al.* 2025). Layering is less evident in this region of low shear near the flow base, where the large-particle volume fraction also appears much smaller.

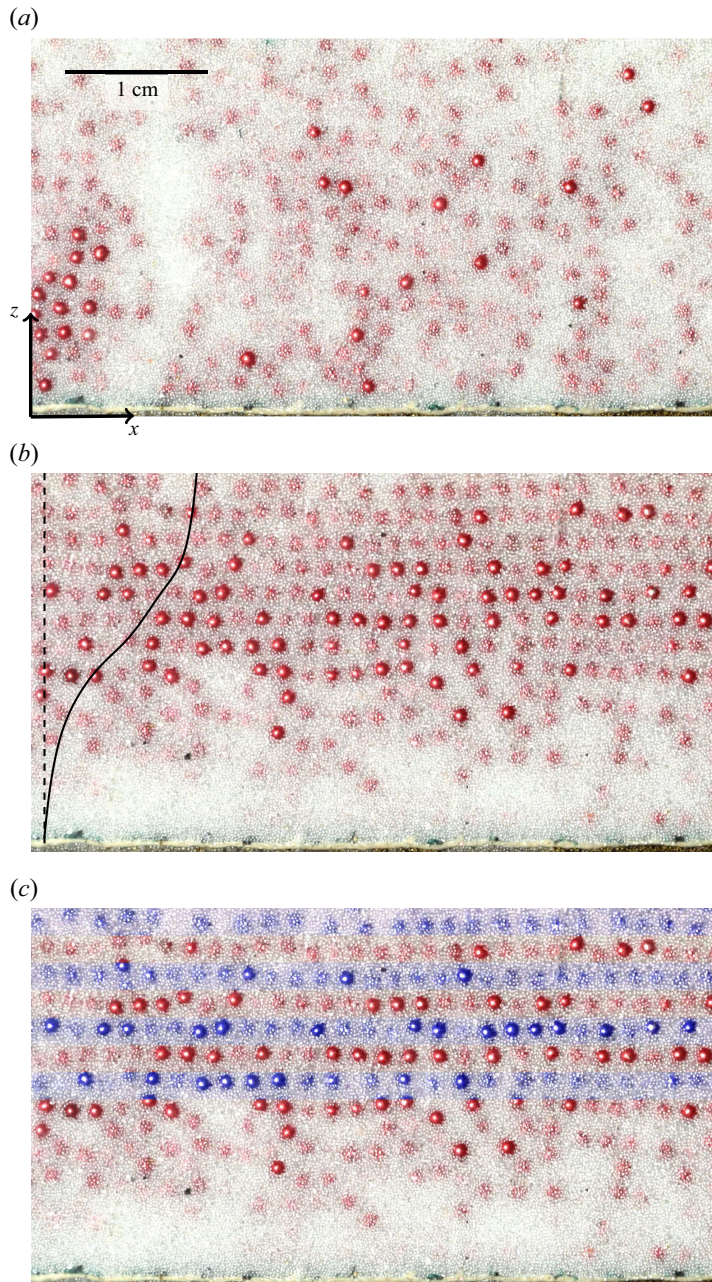


Figure 12. Photographs of the experiment in an inclined rectangular chute. (a) The initial disordered state prior to the onset of flow and (b) the system 11 s after flow has commenced, with large particles forming distinct layers. A sketch of the velocity profile is overlaid. Panel (c) reproduces (b), with eight equally spaced 1.9 mm wide rectangles applied from the top; the hue of alternate rectangles has been shifted to blue to highlight the layered structure that is present in (b). The full time evolution of the layering can be seen at full speed and 1/3 speed in supplementary movies 4 and 5, respectively. The top of the images is 27 mm above the rigid base, placing it approximately halfway between the upper and lower boundary.

At least eight distinct layers of large particles are evident in the central shearing part of the flow, aligned with the velocity gradient, consistent with the layering observed in DEM simulations. Figure 12(c) reproduces figure 12(b) but the hue of the image has been artificially shifted to blue in four rectangles, each 1.9 mm in height and spaced by 1.9 mm (approximately the diameter of one large particle plus the diameter of between one and two small particles). In the resulting image almost all large grains lie either wholly within a red stripe or wholly within a blue stripe, a pattern which emerges because the large particles are arranged into discrete layers. In particular, it shows that the layers remain contiguous over a considerable distance in the flow direction, in figure 12(c) spanning the entire width of the frame of around 28 large particles. As shown in supplementary movies 4 and 5, the number of large particles visible within each layer can exceed 100, indicating that the layering extends well beyond the limited view captured in the static image.

The experiment confirms that layering is not simply a consequence of periodic boundary conditions or finite simulation domains, but is an experimentally realisable phenomenon that is intrinsic to real size-bidisperse granular flows. Layering was consistently observed across multiple repeated experimental runs giving confidence that the effect is robust. Additionally, the alignment of large particles into long chains and the organisation into discrete layers may both have important consequences for the rheology of such flows; however, this paper focuses on the description and modelling of the segregation behaviour.

4. Bulk segregation: governing equations

4.1. Bidisperse mixture framework

The aim is now to model the segregation behaviour in figure 1 within a continuum framework. Consider a granular material composed of large and small particles of the same intrinsic density ρ_* . Each species has diameter d^v , where $v = l, s$ denotes large and small particles, respectively. The solids volume fraction of each species is Φ^v and the total solids volume fraction of the granular material is $\Phi = \Phi^s + \Phi^l$. In dense monodisperse flows (GDR-MiDi 2004) as well as bidisperse flows up to a size ratio $R = 2.5$ (Tripathi & Khakhar 2011), Φ is nearly constant across the flow. Although a bidisperse mixture can pack more densely than monodisperse grains, and these packing effects may become more significant at larger size ratios (Srivastava *et al.* 2021), for simplicity and compatibility with existing segregation theories (e.g. Gray 2018; Umbanhower *et al.* 2019) Φ is here approximated as uniform throughout the flow. Figure 1(b) shows some evidence of volume fraction variation with changes in the free-surface height across different values of $\bar{\phi}^s$. The observed variation is modest, however, at only 5%–10%, and is therefore neglected. As a result, the bulk velocity \mathbf{u} can be approximated as incompressible:

$$\nabla \cdot \mathbf{u} = 0. \tag{4.1}$$

The theory is expressed in terms of the species' concentration $\phi^v \in [0, 1]$, defined, as in § 2, as the volume fraction per unit granular volume,

$$\phi^v = \frac{\Phi^v}{\Phi}, \tag{4.2}$$

such that concentrations sum to unity:

$$\phi^s + \phi^l = 1. \tag{4.3}$$

Segregation is modelled using the well-established framework of advection–segregation–diffusion equations (see e.g. Gray 2018), which governs the spatial and temporal evolution

of the concentrations ϕ^ν through

$$\frac{\partial \phi^\nu}{\partial t} + \underbrace{\nabla \cdot (\phi^\nu \mathbf{u})}_{\text{advection}} + \underbrace{\nabla \cdot \mathbf{F}^\nu}_{\text{segregation}} = \underbrace{\nabla \cdot (D \nabla \phi^\nu)}_{\text{diffusion}}. \tag{4.4}$$

In this framework, the flux of each species is assumed to be composed of three distinct components: an advective flux $\phi^\nu \mathbf{u}$ that simply sweeps species ν along with the bulk flow, a local segregation flux \mathbf{F}^ν that drives different species to different regions of the flow and a diffusive flux $D \nabla \phi^\nu$ that accounts for the fluctuating motion of the grains (Gray & Chugunov 2006), where D is the binary diffusion coefficient.

To close the segregation model, functional forms for the segregation fluxes must be provided, which satisfy a number of constraints. Firstly, in order to satisfy the bulk incompressibility (4.1) the segregation fluxes of large and small particles must sum to zero:

$$\mathbf{F}^s + \mathbf{F}^l = \mathbf{0}. \tag{4.5}$$

This means only a single segregation flux needs to be specified, as the other will be given by (4.5). In this paper, the small-particle segregation flux \mathbf{F}^s is specified. A second constraint requires that segregation shuts off when either constituent is in pure phase. Thus \mathbf{F}^s must vanish when $\phi^s = 0$ and $\phi^s = 1$. The simplest flux function satisfying this constraint was postulated by Dolgunin & Ukolov (1995) and has a quadratic dependence on ϕ^s :

$$\mathbf{F}^s = \phi^s (1 - \phi^s) \mathbf{q}, \tag{4.6}$$

where vector \mathbf{q} has dimensions of velocity and sets the magnitude and the direction of segregation. Experiments, DEM simulations and theoretical analyses of bidisperse mixtures have revealed that \mathbf{q} depends on the diameter ratio $R = d^l/d^s$ between the grains (Thornton *et al.* 2012), small-particle concentration ϕ^s (van der Vaart *et al.* 2015), shear rate $\dot{\gamma}$ (Bridgwater, Foo & Stephens 1985; Savage & Lun 1988; Marks, Rognon & Einav 2012; Fan *et al.* 2014), pressure p (Golick & Daniels 2009; Fry *et al.* 2019; Trehwela *et al.* 2021) as well as gradients of pressure (Gray & Thornton 2005; Staron & Phillips 2015), kinetic stress (Hill & Tan 2014) and shear rate (Jing *et al.* 2021):

$$\mathbf{q} = \mathbf{q}(\phi^s, R, \dot{\gamma}, p, \nabla p, \nabla \dot{\gamma}, \dots). \tag{4.7}$$

A completely general functional form of \mathbf{F}^s is still subject to debate, but so far, models of size-bidisperse grains of equal density have only captured the conventional segregation shown in figure 1(a). This paper presents flux functions with a concentration dependence that allows a unified description of both reverse and standard segregation of large particles.

We examine segregation in a free-surface flow over an inclined plane. To facilitate comparison with the DEM simulations, in which periodic boundary conditions are imposed in the down-slope (x) and cross-slope (y) directions, the flow is assumed to be uniform in the x and y directions, with the only flow gradients occurring in the slope-normal z direction. Under these assumptions the general segregation equation (4.4) simplifies to

$$\frac{\partial \phi^s}{\partial t} + \frac{\partial F^s}{\partial z} = \frac{\partial}{\partial z} \left(D \frac{\partial \phi^s}{\partial z} \right), \tag{4.8}$$

where F^s is the z component of \mathbf{F}^s . This is subject to the boundary condition of no flux of particles through the base at $z = 0$ and the free surface at $z = h$:

$$F^s = D \frac{\partial \phi^s}{\partial z} \quad \text{on } z = 0, h. \tag{4.9}$$

Integrating (4.8) between the base and free surface and applying (4.9) implies

$$\frac{\partial \overline{\phi^s}}{\partial t} = 0, \tag{4.10}$$

where

$$\overline{\phi^s} = \frac{1}{h} \int_0^h \phi^s dz \tag{4.11}$$

is the mean fraction of small particles throughout the flow depth. Seeking steady solutions to the partial differential equation (4.8) simplifies it to an ordinary differential equation (ODE). Integrating (4.8) in z and applying (4.9) then gives

$$\frac{d\phi^s}{dz} = \frac{F^s}{D}. \tag{4.12}$$

This expresses the gradient of the concentration profile as a balance between segregation and diffusion. Integrating (4.12) once more to obtain a unique solution for $\phi^s(z)$ requires an additional constraint, for which the constant $\overline{\phi^s}$ is specified. It also requires explicit expressions for F^s and D , which are the focus of § 5.

The ODE (4.12) subject to the integral constraint (4.11) is solved by introducing the potential ψ , defined as

$$\psi(z) = \frac{1}{h} \int_0^z \phi^s(z') dz'. \tag{4.13}$$

This satisfies the ODE

$$\frac{d\psi}{dz} = \frac{\phi^s}{h}, \tag{4.14}$$

and boundary conditions

$$\psi(0) = 0 \quad \text{and} \quad \psi(h) = \overline{\phi^s}. \tag{4.15}$$

Equations (4.12) and (4.14) and boundary conditions (4.15) form a two-point boundary-value problem for ϕ^s , which is solved by shooting.

5. Bidirectional segregation flux

5.1. Neutral concentration

Recall that at size ratios $R \geq 4$, large particles tend to sink to the base of the flow when present in low concentrations (reverse segregation). This contrasts with the segregation behaviour at $R \leq 4$ where large particles rise to the surface irrespective of their concentration, leading to the large particles overlaying smaller particles. Current continuum models for segregation have been constructed for $R \leq 4$; consequently their small-particle segregation fluxes F^s are always negative to ensure small particles are transported towards the base, and large particles rise to the surface. This renders them incapable of predicting segregation at larger size ratios. To address reverse segregation, a form F^s is proposed that becomes negative for high concentrations of small particles, at size ratios large enough for reverse segregation to occur.

To begin, the small-particle segregation flux F^s , in the limit of a single small or single large intruder, is examined. These limits correspond to the small-particle concentrations $\phi^s = 0^+$ and $\phi^s = 1^-$, respectively, where the superscripts ‘+’ and ‘-’ denote concentrations just above or below 0 and 1.

A single small intruder ($\phi^s = 0^+$) will percolate downwards through a shearing matrix of large particles under the action of gravity, resulting in a downward flux of small particles, $F^s < 0$. Conversely, for $R \gtrsim 4$ a single large intruder ($\phi^s = 1^-$) will sink under gravity (Thomas & D’Ortona 2018). This results in a downward flux of large particles. By the mass conservation condition (4.5), there must be an upward flux of small particles relative to the bulk flow, $F^s > 0$. In particular, there is a change in sign of the segregation flux F^s as the concentration moves from zero to one. Importantly, this suggests that there is some intermediate concentration, denoted the neutral concentration, ϕ_n^s , at which $F^s = 0$:

$$F^s(\phi_n^s) = 0. \tag{5.1}$$

The above reasoning constrains F^s to have at least one root. However, F^s must also vanish in the monodisperse limits $\phi^s = 0, 1$, where segregation shuts off. The simplest form of F^s that has three roots at $\phi^s = 0, \phi_n^s$ and 1 has a cubic concentration dependence:

$$F^s = q\phi^s(1 - \phi^s)(\phi_n^s - \phi^s), \tag{5.2}$$

where q is a negative parameter with dimensions of velocity that sets the rate of segregation, analogously to (4.6). The parameter q may also depend on flow variables and particle properties as per (4.7).

The neutral concentration ϕ_n^s is the concentration at which segregation reverses. It determines whether large particles rise or sink within the flow. For $\phi^s < \phi_n^s$ the large particles rise to the surface. For $\phi^s > \phi_n^s$ the large particles sink towards the base. Between these cases there lies a third, intermediate regime where $\phi^s = \phi_n^s$ and $F^s = 0$, in which there is no net movement of large particles. This corresponds to $\phi^s \approx 0.6$ in figure 2(b) where ϕ^s becomes almost uniform with depth.

The value of ϕ_n^s will depend upon the size ratio R , since the small-particle concentration at which segregation reverses decreases with R (figure 4, and Thomas & D’Ortona 2018). In particular, for $R \lesssim 4$ no reversal in segregation has been observed (Thomas & D’Ortona 2018), so the segregation flux F^s must remain negative on the interval $\phi^s \in (0, 1)$. From the form (5.2) of F^s , this requires $\phi^s < \phi_n^s$ throughout this range. Furthermore, given that the direction of segregation does reverse for $R \gtrsim 4$, the neutral concentration must obey

$$\phi_n^s > 1 \quad \text{for} \quad 1 \leq R \lesssim 4 \tag{5.3}$$

and

$$0 < \phi_n^s \leq 1 \quad \text{for} \quad R \gtrsim 4. \tag{5.4}$$

The introduction of the neutral concentration ϕ_n^s has a significant impact on the segregation flux (figure 13). When $\phi_n^s > 1$ the segregation flux is skewed relative to the symmetric, quadratic model (figure 13a) with its minimum shifted towards lower small-particle concentrations (figure 13b). As ϕ_n^s decreases towards unity, F^s becomes increasingly asymmetric. When ϕ_n^s drops below one, a new root appears at $\phi^s = \phi_n^s$ (figure 13c), marking a qualitative change in behaviour. In this regime F^s can take either sign: it is negative for $\phi^s < \phi_n^s$, indicating small particles moving downwards, and it is positive for $\phi^s > \phi_n^s$, representing small particles being pushed upwards. This is in stark contrast to the case with $\phi_n^s > 1$, where F^s is always negative to ensure small particles are transported towards the base.

Asymmetric segregation fluxes such as that shown in figure 13(b) have previously been proposed by Gajjar & Gray (2014) in order to model the asymmetry in segregation rates between small and large particles. Specifically, in the regime where large particles rise to the surface, a lone small particle will typically migrate downwards through a matrix of

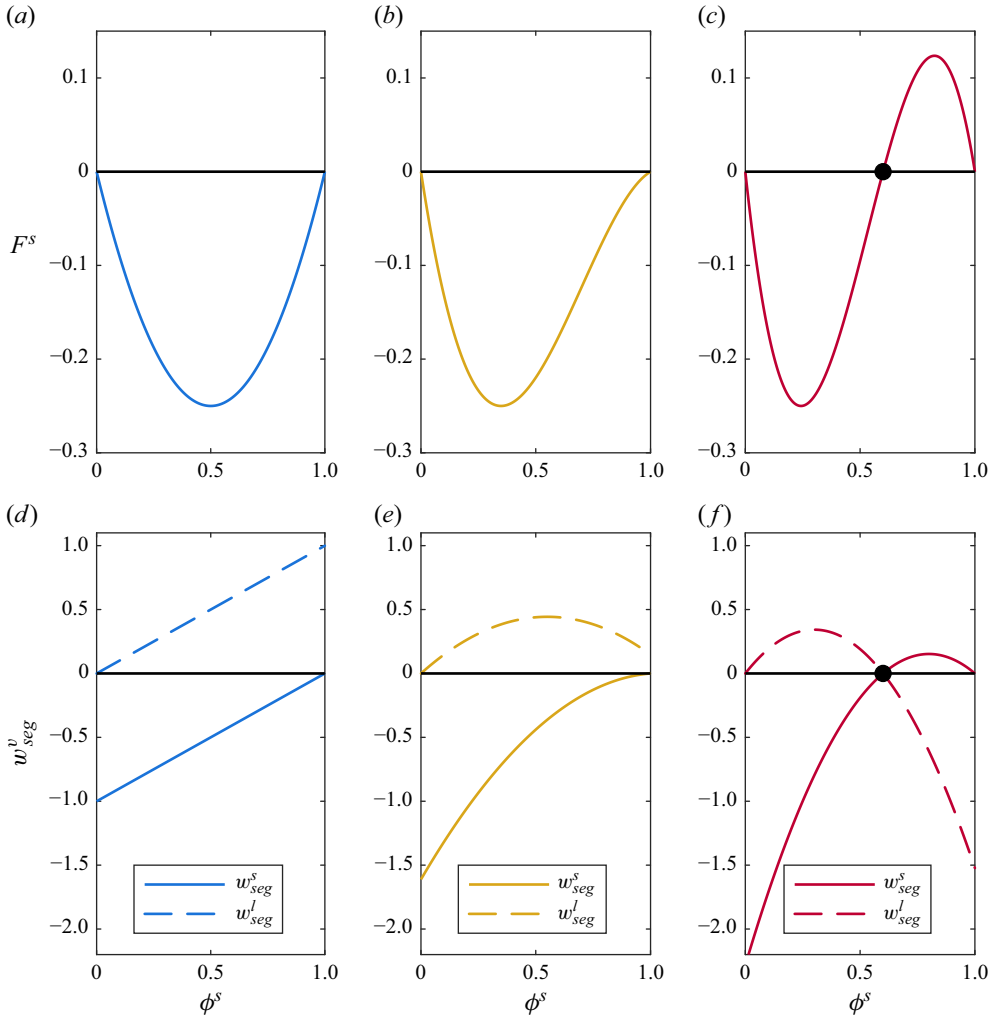


Figure 13. Schematic plots of (a–c) the small-particle segregation flux, F^s , as a function of small-particle concentration, ϕ^s . Curve (a) corresponds to the symmetric, quadratic model (4.6); curve (b) shows a strictly negative cubic flux based on (5.2) with $\phi_n^s = 1.1$; and curve (c) depicts a bidirectional cubic flux from (5.2) with $\phi_n^s = 0.6$. All fluxes plotted here share the same maximum magnitude, $|F^s| = 0.25$; the dependence of this magnitude on flow variables is discussed separately in § 5.2. (d–f) The normal segregation velocities of small (5.5) and large (5.6) particles, corresponding to the fluxes in (a–c), respectively. The black circles in (c, f) mark the neutral concentration $\phi_n^s = 0.6$, the concentration at which segregation reverses.

large particles more quickly than a large particle rises through a matrix of small particles (van der Vaart *et al.* 2015). This asymmetry is not captured by the quadratic flux (4.6), which is symmetric about a 50 % concentration of small particles (figure 13a).

The effect of skewing the flux can be seen in the small- and large-particle segregation velocities, defined by

$$w_{seg}^s = w^s - w = \frac{F^s}{\phi^s} = q(1 - \phi^s)(\phi_n^s - \phi^s), \quad (5.5)$$

$$w_{seg}^l = w^l - w = -\frac{F^s}{1 - \phi^s} = -q\phi^s(\phi_n^s - \phi^s). \quad (5.6)$$

Here, w^v is the slope-normal, z , component of the velocity of species v and $w = \phi^s w^s + \phi^l w^l$ is the bulk z velocity. A positive segregation velocity ($w_{seg}^v > 0$) indicates that species v is segregating upwards, while a negative value indicates downward segregation. For the symmetric flux function, the segregation velocity for a single small intruder ($\phi^s = 0^+$) and the segregation velocity for a single large intruder ($\phi^s = 1^-$) are equal in magnitude (figure 13*d*). In the skewed case (figure 13*e*), however, the segregation velocity of a small intruder is larger in magnitude than that of a large intruder, reflecting the asymmetry in the underlying flux.

Gajjar & Gray (2014) restricted their model to negative F^s to ensure that small particles always segregate downwards, which corresponds to the neutral concentration taking values $\phi_n^s \geq 1$. Allowing the neutral concentration ϕ_n^s to take values on the interval $(0, 1)$ introduces a bidirectional flux with segregation velocities that change sign at $\phi^s = \phi_n^s$ (figure 13*f*). In this regime, both small and large intruders exhibit downward segregation, unlike the case where $\phi_n^s \geq 1$. Thus, the cubic flux form (5.2) may be considered as a natural extension of the model of Gajjar & Gray (2014) to larger size ratios, that is able to capture both the asymmetry in the segregation rates and the reversal in the segregation direction, depending on the value of the neutral concentration ϕ_n^s . Although a cubic dependence on ϕ^s is the simplest form capable of capturing either the asymmetry in segregation rates or a reversal in segregation direction, the segregation flux F^s may, in general, be a more complicated function of ϕ^s .

The proposed model (5.2) has a mathematical structure similar to combined size and density models that allow for a concentration-dependent reversal in the segregation direction (Gray & Ancey 2015; Duan *et al.* 2021). In these models, large particles that are denser than the small ones may sink when present in low concentrations but rise when present in high concentrations. This reversal arises because different segregation mechanisms dominate at different concentrations: at low concentrations, buoyancy effects make isolated dense large particles sink, while at high concentrations, the downward migration of small particles through voids drives the dense large particles upward. The analogous mathematical form of the segregation flux may reflect a similar underlying mechanism for the reversal at large size ratios. An isolated large particle, even if it has the same intrinsic density as the small particles, can sink because it is effectively denser, relative to the surrounding mixture of small particles and void space. At higher concentrations of large particles, however, this effective density contrast is reduced, and the segregation is instead controlled by small particles falling downward through voids, which displaces the large particles upward.

5.2. Flow dependence

5.2.1. Diffusion

In steady state, (4.12) implies that the concentration profile is determined by a balance between the local segregation flux and the diffusive flux. Diffusion in granular flows is driven by shear, with regions of higher shear rate experiencing larger fluctuations leading to enhanced diffusion. In monodisperse flows, the grains undergo Fickian (normal) diffusion, and dimensional analysis requires the diffusion coefficient D to be of the form (Bridgwater 1980; Savage & Dai 1993; Utter & Behringer 2004)

$$D = \dot{\gamma} d^2 D_0(I), \tag{5.7}$$

where D_0 is, in general, an arbitrary function of the inertial number

$$I = \frac{\dot{\gamma} d}{\sqrt{p/\rho_*}}. \tag{5.8}$$

For $I \geq 0.1$ the dependence of D_0 on I is weak; however, at very low inertial numbers the diffusivity increases more strongly, scaling as $D \propto I^{-1/2}$ (Kharel & Rognon 2018).

Cai *et al.* (2019) extended expressions for self-diffusion in monodisperse flows to bidisperse systems up to a size ratio $R = 3$ by replacing the particle diameter d with the volume-weighted mean particle diameter \bar{d} :

$$\bar{d} = \phi^s d^s + \phi^l d^l. \quad (5.9)$$

This ensures that when the flow is dominated by small particles ($\phi^s = 1$), \bar{d} reduces to the small-particle diameter d^s , and when the flow is dominated by large particles ($\phi^s = 0$), \bar{d} equals the large-particle diameter d^l . This results in an average diffusion coefficient

$$D = D_0 \dot{\gamma} (\bar{d})^2, \quad (5.10)$$

where $D_0 \in (0.03, 0.05)$ is approximately constant, although there is a weak dependence on the volume fraction (Cai *et al.* 2019). This is consistent with the results of multiple studies using monodisperse grains (Bridgwater 1980; Savage & Dai 1993; Campbell 1997; Bancroft & Johnson 2021). In this study, a diffusion coefficient $D_0 = 0.04$ is used, as in Maguire *et al.* (2024).

5.2.2. Segregation flux

Up to this point, only the minimal concentration dependence of the segregation flux required to capture the reverse segregation of large particles has been considered. However the segregation flux may have further dependence on ϕ^s as well as on flow variables and particle properties. Concentration dependence alone has been shown to provide an effective approximation to the segregation profiles at $R = 2$ (Wiederseiner *et al.* 2011); however, a more complete segregation model requires incorporating additional dependences. These enter the segregation flux through the segregation rate q in (5.2).

Through the use of shear box experiments to examine the single intruder limit of segregation, Trewhela *et al.* (2021) determined that q is linear in the shear rate $\dot{\gamma}$ and inversely proportional to the pressure p . This relationship can be primarily attributed to the drag on segregating particles (Bancroft & Johnson 2021; Jing *et al.* 2022). In free-surface flows over an inclined plane, which is the configuration considered in this paper, the normal segregation force due to the hydrostatic pressure gradient dominates over that due to the shear rate gradient (Jing *et al.* 2021). These findings suggest that the segregation flux can be expressed as

$$F^s = \frac{\dot{\gamma} (\bar{d})^2}{p} \frac{dp}{dz} f(\phi^s, R), \quad (5.11)$$

where the hydrostatic pressure for a flow of height h on a plane inclined at angle θ is given by

$$p = \rho_* \Phi g \cos \theta (h - z), \quad (5.12)$$

and where \bar{d} is chosen as a reference length scale (Trewhela *et al.* 2021). The function $f(\phi^s, R)$ encapsulates the concentration dependence of the segregation flux, as was discussed in § 5.1. It is expected that f is positive for $R \lesssim 4$ to ensure that small particles migrate downwards. To model reverse segregation, f must be at least a cubic in ϕ^s , though higher-order forms are possible. In this paper a cubic form is primarily considered, as it provides the simplest model with the necessary properties:

$$f_3(\phi^s, R) = A \phi^s (1 - \phi^s) (\phi_n^s - \phi^s). \quad (5.13)$$

This function vanishes at $\phi^s = 0, 1$ as required, and is characterised by two dimensionless parameters: a constant overall amplitude A which scales the strength of segregation and the neutral concentration ϕ_n^s which sets the point of reversal. Both parameters depend on the size ratio R and are determined by fitting to the data from DEM simulations. For comparison, a quintic form of f is also considered:

$$f_5(\phi^s, R) = B_1\phi^s(1 - \phi^s)(B_2 - \phi^s)(1 + B_3\phi^s + B_4\phi^s{}^2), \quad (5.14)$$

which allows quantitative concentration profiles to be captured more accurately. However, this comes at the expense of using four dimensionless parameters compared with two for the cubic model. These parameters are denoted B_1, B_2, B_3 and B_4 and depend on the size ratio R . The amplitude of the flux function is controlled by B_1 , while B_2 sets the concentration at which segregation reverses. The remaining parameters, B_3 and B_4 , adjust the curvature of the flux function, enabling a closer match to DEM profiles.

5.3. Steady state

Substituting the forms of the segregation flux and diffusive flux into the equation for the steady-state concentration profiles (4.12) results in

$$\frac{d\phi^s}{dz} = \frac{-f(\phi^s, R)}{D_0(h - z)}. \quad (5.15)$$

Since both the segregation flux F^s and the diffusive flux are linear in the shear rate, the shear rate dependence is removed in steady state, and thus the steady-state profiles are not dependent on the rheology. This equation is integrated between the base $z = 0$ and the free surface $z = h$ subject to the constraint (4.11) on the depth-averaged concentration of small particles.

By inspection, one solution of (5.15) is $\phi^s = \phi_n^s$, corresponding to well-mixed particles with a uniform vertical distribution. The model therefore predicts the complete suppression of segregation in such mixtures, corresponding to the vertical dashed line in figure 2(b), which is approximately equal to the results of the DEM simulation at $\bar{\phi}^s = 0.6$ through the majority of the flow depth. This divides other solutions of (5.15) into two classes: those for which $\phi^s < \phi_n^s$ for all z and those for which $\phi^s > \phi_n^s$ for all z . For both classes, there is a singularity in (5.15) at $z = h$, which arises because the pressure vanishes at the free surface, causing the segregation flux F^s to diverge as z approaches h . This divergence in F^s forces each species into pure phase at the free surface ($\phi^s = 0$ or $\phi^s = 1$ at $z = h$), a prediction in good agreement with the results of the DEM simulations in figure 2.

6. Comparison with DEM

The segregation model (5.15) with both cubic and quintic flux functions is now compared with the results of our inclined-plane DEM simulations. The free parameters in the model (A and ϕ_n^s for the cubic and B_1, B_2, B_3 and B_4 for the quintic) are determined by fitting directly to all the concentration profiles obtained at 25° simultaneously, for each of $R = 3$ and $R = 6$. All the DEM simulations shown in figure 2, spanning the full range of small-particle fractions $0.1 \leq \bar{\phi}^s \leq 0.9$, are used in the fitting. Parameters are estimated by minimising the total least-squares distance between the model's steady state and the corresponding DEM concentration profile (using MATLAB's `fminsearch`). For each trial parameter set, (5.15) is solved numerically and the resulting profile, which has a nonlinear dependence on the parameters to be fitted, is compared pointwise with the DEM data. To reduce the influence of correlations introduced by the coarse-graining

Function	Parameter	$R = 3$	$R = 6$
f_3 cubic	A	0.132	0.310
f_3 cubic	ϕ_n^s	1.28	0.597
f_5 quintic	B_1	0.600	0.600
f_5 quintic	B_2	1.14	0.632
f_5 quintic	B_3	-2.94	-3.61
f_5 quintic	B_4	2.66	4.75

Table 1. Fitted parameters for the cubic flux function f_3 and the quintic flux function f_5 at $R = 3$ and $R = 6$.

procedure, data points used in the least-squares fit are spaced by $3d^s$ for $R = 3$ and $5d^s$ for $R = 6$, ensuring each point is separated by more than one coarse-graining width. The fitted parameter values for both models are listed in [table 1](#).

The results of the segregation model are compared with the DEM concentration profiles for different small-particle fractions $\bar{\phi}^s$ at $R = 3$ in [figure 14](#) and at $R = 6$ in [figure 15](#). For each of the nine values of $\bar{\phi}^s$, ranging from 0.1 to 0.9, the same set of fitted parameters is used. Remarkably, the simple cubic flux function, with only two free parameters, is sufficient to quantitatively reproduce the range of segregation behaviours observed across both size ratios. The quintic model, which introduces two additional fitting parameters, is qualitatively unchanged, but provides an improved fit, as expected.

The neutral concentration ϕ_n^s plays a key role in shaping the concentration profiles. For size ratio $R = 3$, the fitted value $\phi_n^s = 1.28$ exceeds one, indicating that large particles tend to accumulate near the surface. In contrast, at $R = 6$, $\phi_n^s = 0.597$, and surface composition depends on the small-particle fraction $\bar{\phi}^s$; when $\bar{\phi}^s < \phi_n^s$, large particles rise to the surface and when $\bar{\phi}^s > \phi_n^s$, small particles lie on the surface.

This dependence is shown in [figure 15\(f\)](#) at $\bar{\phi}^s = 0.6$, where the cubic model captures the near-uniform concentration in the bulk, but differs from the DEM data at the free surface. The model places small particles at the surface, consistent with $\phi_n^s = 0.597 < 0.6$, while the DEM shows large particles on top, a discrepancy arising from a difference of just 0.5 % in the fitted value of ϕ_n^s . By contrast, the quintic model uses the parameter B_2 , which plays an analogous role to ϕ_n^s , and has a fitted value of $B_2 = 0.632 > 0.6$; it therefore correctly predicts the composition at the free surface in all of the simulations.

The inverse dependence of the segregation flux on the pressure also plays an important role in shaping the concentration profiles. Near the base of the flow, where the pressure is highest, segregation is relatively weak, leading to more gradual variation in mixture composition. In contrast, near the free surface, where the pressure approaches zero, segregation becomes significantly stronger, driving a rapid transition from a mixed region to one dominated by either pure large or pure small particles. This sharp segregation near the surface is most evident in [figure 14\(g-i\)](#).

A more direct approach to validating the model is to measure the segregation flux function $f(\phi^s, R)$ directly from the DEM simulations and compare it with the cubic/quintic fluxes chosen in the theory, rather than fitting and comparing the concentration profiles. Starting from the steady-state ODE for ϕ^s ([5.15](#)), the flux can be expressed as

$$f(\phi^s, R) = -D_0 \frac{d\phi^s}{dz}(h - z), \tag{6.1}$$

where the dimensionless diffusion coefficient $D_0 = 0.04$, and the other terms on the right-hand side can be evaluated from the DEM data. The concentration gradient $d\phi^s/dz$ is

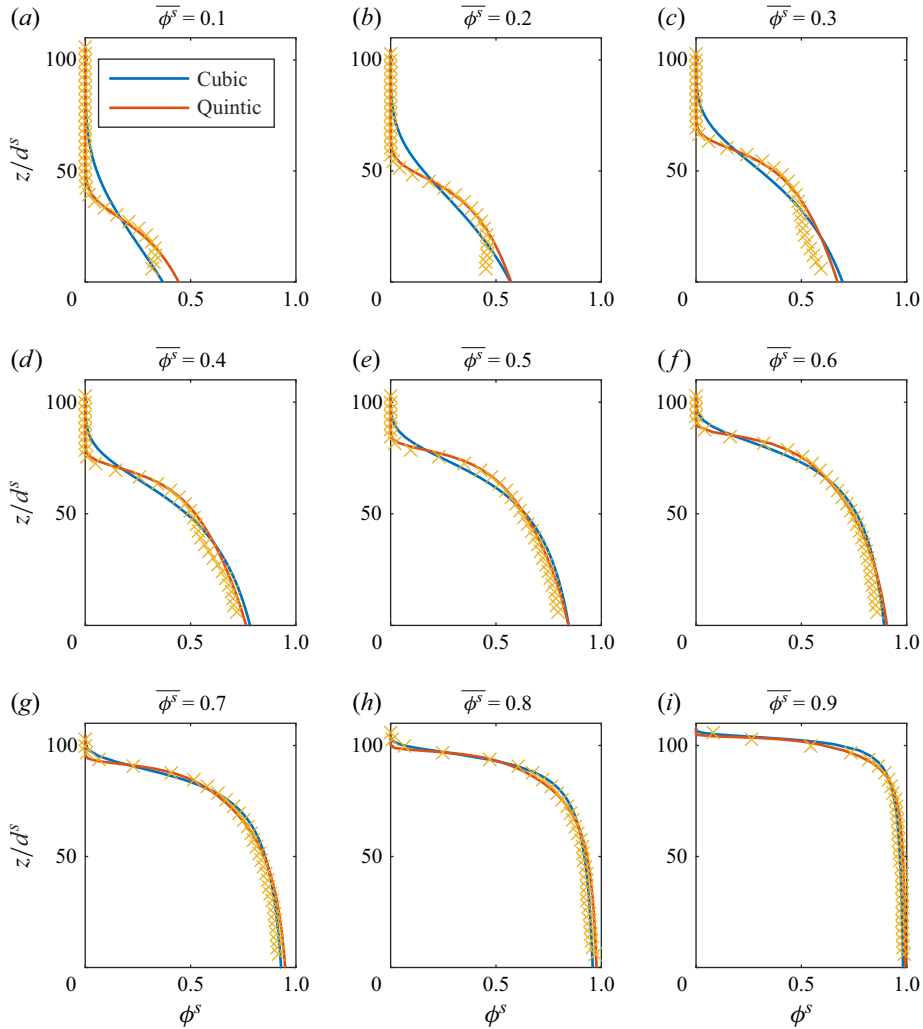


Figure 14. Comparison of concentration profiles for a size ratio of $R = 3$ from DEM simulations on a plane inclined at 25° (crosses) and the predictions of the segregation model (5.15), using a cubic flux function f_3 (blue line) and a quintic flux function f_5 (red line). The panels span small-particle fractions $\bar{\phi}^s$ from (a–i) 0.1 to 0.9, in increments of 0.1.

estimated from the coarse-grained ϕ^s profiles using centred finite differences:

$$\frac{d\phi^v}{dz} \approx \frac{\phi^v(z + \Delta z) - \phi^v(z - \Delta z)}{2\Delta z}, \quad (6.2)$$

with step size $\Delta z = d^s$.

Figure 16 plots $-f(\phi^s, R)$ against ϕ^s for both $R = 3$ and $R = 6$, using data from multiple simulations (different values of $\bar{\phi}^s$) and different heights z within the flow. According to (6.1), f should be independent of the height z for fixed ϕ^s , so data points collected at different vertical locations should collapse onto a single curve. This collapse is broadly observed in the data despite some scatter, which occurs particularly for low concentrations of small particles at $R = 6$. The greater scatter at low ϕ^s may reflect additional physics not captured by the model. For instance, $R = 6$ is close to the

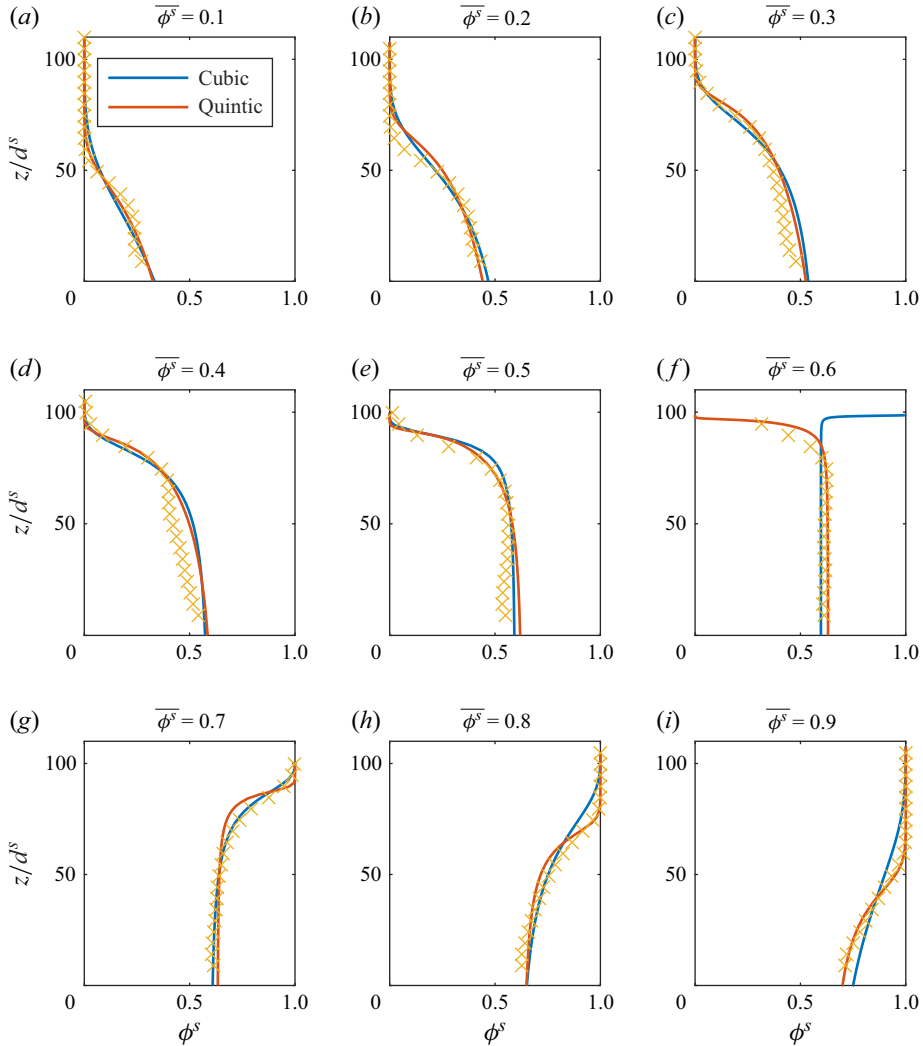


Figure 15. Comparison of concentration profiles for a size ratio of $R = 6$ from DEM simulations on a plane inclined at 25° (crosses) and the predictions of the segregation model (5.15), using a cubic flux function f_3 (blue line) and a quintic flux function f_5 (red line). The panels span small-particle fractions ϕ^s from (a–i) 0.1 to 0.9, in increments of 0.1.

threshold for spontaneous percolation (Wilkinson & Edwards 1982) where the segregation velocity can be independent of the shear rate (Gao *et al.* 2024). Variations in the pressure dependence of the segregation flux in this regime may also contribute. Alternatively, some of the observed scatter may be attributed to numerical sensitivity; because the flux is computed using concentration gradients, even small local fluctuations in ϕ^s can lead to amplified noise.

Both the cubic and quintic flux functions (using the fitted parameters from table 1) qualitatively capture the overall shape of the segregation flux. For $R = 3$, both forms are negative and skewed towards low ϕ^s , consistent with the DEM data in figure 16(a). For $R = 6$, both functions exhibit a root near $\phi^s \approx 0.6$, matching the reversal point observed in figure 16(b). However, the quintic form better reproduces the curvature and detailed structure of the DEM-extracted flux function.

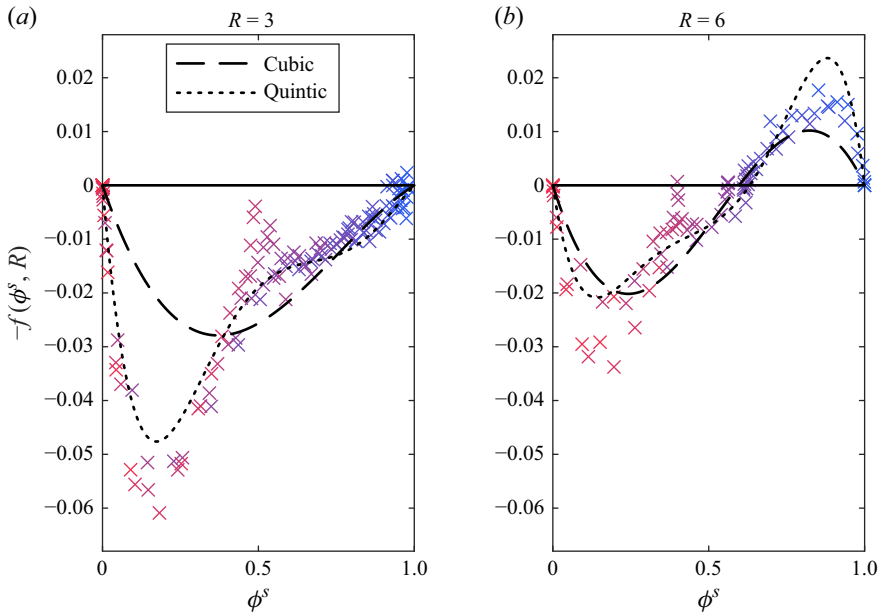


Figure 16. Negative of the flux function, $-f(\phi^s, R)$, plotted as a function of small-particle concentration ϕ^s for (a) $R = 3$ and (b) $R = 6$. Crosses represent values of $f(\phi^s, R)$ extracted from DEM simulations by evaluating the product of $D_0, (h - z)$ and $d\phi^s/dz$, as given in (6.1). Colours denote different bulk small-particle fractions $\bar{\phi}^s$, ranging from 0.1 (red) to 0.9 (blue), with data sampled at various heights within the flow. Points are spaced at intervals of $3d^s$ for $R = 3$ and $5d^s$ for $R = 6$ to ensure a separation greater than the coarse-graining width. These measurements are compared with the cubic (5.13) and quintic (5.14) flux functions, using the fitted parameters listed in table 1.

An important feature revealed by this analysis is that the magnitude of the flux is significantly larger for $R = 3$ than for $R = 6$ (figure 16), indicating weaker segregation at higher size ratios. This aligns with previous observations that the segregation rate peaks at intermediate size ratios (typically around $R \approx 2$) and diminishes at larger R (Thornton *et al.* 2012). The data presented here are consistent with this trend and provide further evidence that the strength of segregation declines beyond the peak, resulting in greater mixing at larger size ratios.

The continuum model (5.15) is now compared with results from DEM simulations conducted at slope angles of 23° and 27° (figure 17) using the same parameters given in table 1. For monodisperse grains with the same frictional and material properties described in § 2.1, these angles correspond to inertial numbers in the range $0.09 < I < 0.24$, based on calibrating the $\mu(I)$ rheology of Jop *et al.* (2005) to this material. This range spans much of the dense inertial regime. For slopes steeper than 28° , the flow can become unstable and fail to reach a steady state (Silbert *et al.* 2001).

The segregation model developed here predicts a steady state that is independent of slope angle, an approximation that performs well when compared with DEM simulations. As shown in figure 17, the model continues to capture the concentration profiles across a range of small-particle fractions $\bar{\phi}^s$ for both $R = 3$ and $R = 6$. The current formulation therefore offers a robust first approximation, although a model incorporating a more complex dependence on shear rate and pressure may yield improved accuracy at varying slope angles.

By way of summary, the continuum model can also be directly compared with the segregation patterns observed in figure 1, as shown in figure 18. The model (5.15) is solved

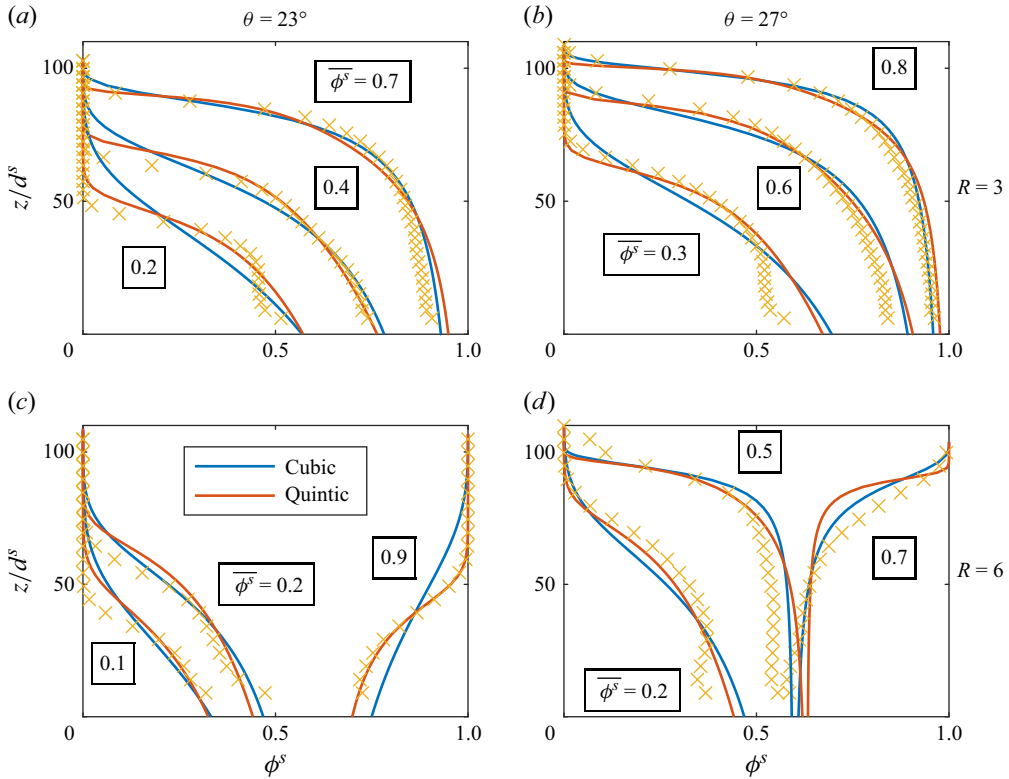


Figure 17. Comparison between concentration profiles from inclined-plane DEM simulations (crosses) and predictions of the segregation model (5.15), using a cubic flux function f_3 (blue line) and a quintic flux function f_5 (red line). The small-particle fractions ϕ^s are indicated on each plot. Results (a) for size ratio $R = 3$ at angle $\theta = 23^\circ$, (b) for $R = 3$ at $\theta = 27^\circ$, (c) for $R = 6$ at $\theta = 23^\circ$ and (d) for $R = 6$ at $\theta = 27^\circ$. The angles $\theta = 23^\circ$ and 27° correspond to inertial numbers $I = 0.09$ and $I = 0.24$, respectively, for monodisperse grains with the same frictional properties described in § 2.1.

for $R = 3$ and $R = 6$, and the resulting concentration profiles are plotted as functions of height z and the bulk small-particle fraction ϕ^s . For $R = 3$, both the DEM snapshots and the continuum solution (figure 18a,b) show large particles consistently accumulating at the surface across all values of ϕ^s . The red triangular region in the top left of each panel indicates the monodisperse region of large particles. In contrast, at $R = 6$, red and grey triangles appear in the top left and right corners, respectively (figure 18c,d), indicating that either large or small particles accumulate at the surface depending on ϕ^s . This shift reflects the change in the direction of the segregation flux across the neutral concentration ϕ_n^s , and the model's ability to capture both types of segregation within a single framework.

7. Summary and conclusions

This paper has investigated the segregation behaviour of size-bidisperse mixtures flowing down an inclined plane for size ratios $2 \leq R \leq 7$, with a focus on $R = 3$ and $R = 6$. A continuum model has been proposed that significantly extends previous models for size segregation, developed for $R \lesssim 3$, to capture the qualitatively different behaviour present at larger R . These include a reversal in the direction of segregation and the existence of approximately uniform, unsegregated states. Despite their relevance to many natural and industrial systems, mixtures with large size ratios remain poorly understood and present

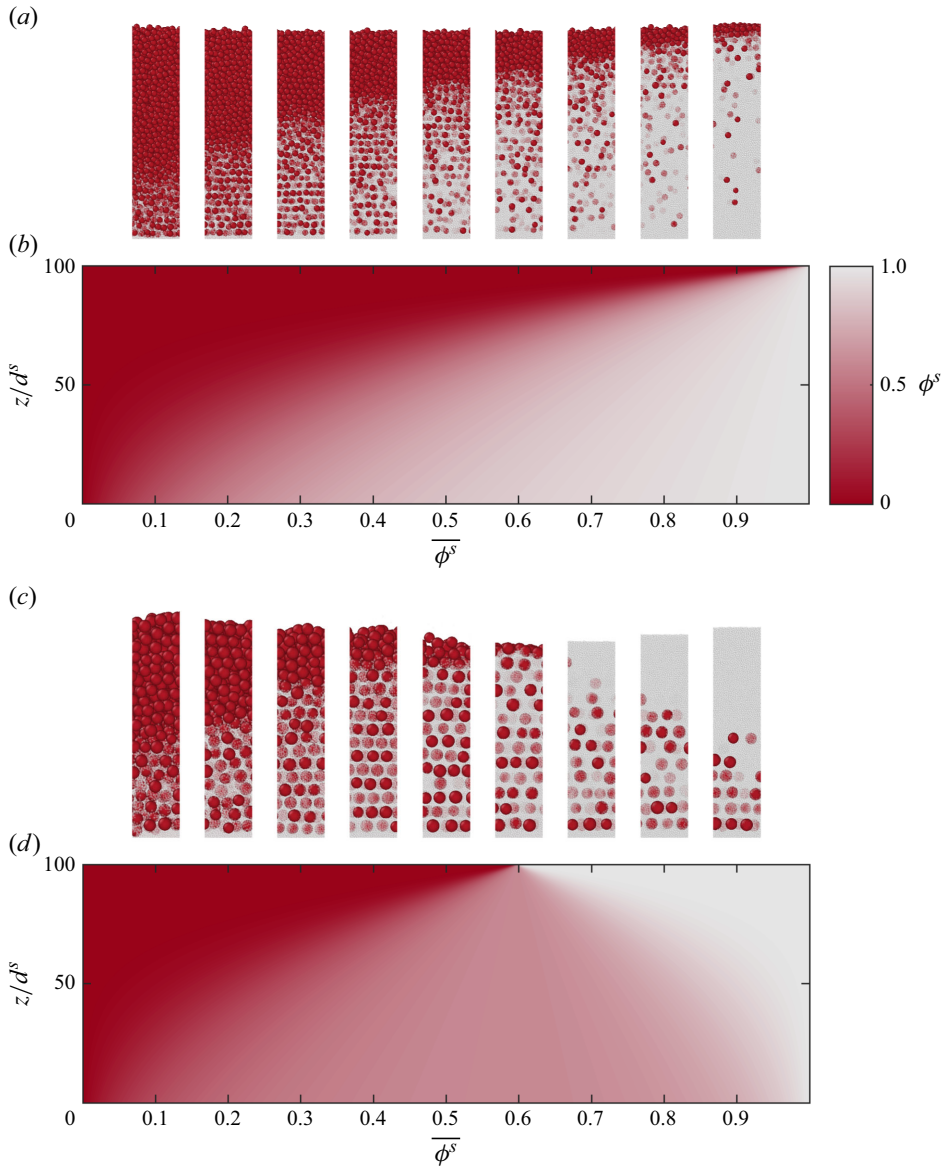


Figure 18. A comparison between DEM snapshots and continuum model predictions at $R=3$ and $R=6$. Panel (a) reproduces the DEM snapshots of figure 1 at $R=3$ and small-particle fractions $\overline{\phi^s}$ increasing from 0.1 to 0.9 in increments of 0.1. (b) The continuum solution for the small-particle concentration as a function of height z and $\overline{\phi^s}$ at $R=3$. This is obtained by solving the segregation model (5.15) with flux function f_3 (5.13) and parameters in table 1. The images in (a) are aligned above their corresponding $\overline{\phi^s}$ values in (b) to enable direct comparison between the DEM images and continuum solution. (c,d) The corresponding results for $R=6$.

substantial modelling challenges. It has also been shown that the large particles self-organise into distinct layers at large size ratios and direct experimental evidence of this layering has been provided for the first time.

One important feature that emerges at $R=6$, but is absent at $R=3$, is the reverse segregation of large particles (Thomas 2000). When large particles are present in low concentrations, they tend to sink towards the base of the flow leaving a surface layer of

small particles, contrary to the upward migration typically observed at smaller size ratios. In this paper, it is shown that as the small-particle fraction $\bar{\phi}^s$ decreases (and hence the large-particle fraction increases) the large particles accumulate progressively from the base upward (figure 1b). At some intermediate $\bar{\phi}^s$, the large particles have filled up from the base to the surface resulting in an approximately homogeneous mixture of large and small particles throughout the flow (figure 2b). At lower values of $\bar{\phi}^s$ the large particles form a surface layer reminiscent of conventional segregation at smaller size ratios. However, even in these cases, the mixture remains well mixed in the region below the large-particle surface.

Computation of the flux function (figure 16) and inspection of the concentration profiles (figures 2 and 18) show that segregation is significantly weaker at $R = 6$ compared with $R = 3$. This is consistent with the observations of Thornton *et al.* (2012) who reported that the strength of segregation has a maximum at $R \approx 2$ and appears to decrease thereafter. Moreover, a neutral concentration ϕ_n^s has been identified at which the strength of segregation is zero, and no segregation occurs. The ability to suppress segregation by increasing the particle size ratio, and eliminate it almost entirely by choosing a small-particle fraction around the neutral concentration ϕ_n^s , opens an avenue for mitigating segregation in industrial flows. Since segregation has long been costly to a number of industries by reducing product uniformity and forcing batches to be discarded, the enhanced mixing observed at large size ratios could offer substantial industrial benefits.

One of the most striking features of flows with large size ratios is the emergence of pronounced layering of large particles (see figures 1, 3, 5, 8 and 12, as well as supplementary movies 1, 2, 4 and 5). Although there is some evidence of layering at $R = 3$, the layers appear more diffuse and are present over a narrower range of small-particle concentrations ϕ^s than at larger size ratios. The layers are exactly one large particle thick and are arranged in the direction of the velocity gradient. Within each layer, the large particles tend to form long chains aligned with the flow direction. In the layered structure, the large particles do not appear to make contact with each other; instead they are separated by thin regions of 1–3 small particles. The layering disappears in nearly monodisperse regions of large or small particles suggesting the layering is distinct from crystallisation. Simulations in a gravity-free, fully periodic Lees–Edwards cell showed that the layering is driven by shear and is not reliant on rigid boundaries. Clear experimental evidence of layering has also been obtained, as shown in figure 12 and supplementary movies 4 and 5, in an inclined rectangular chute. This is the first experimental evidence of layering and confirms that it is a genuine intrinsic feature of sheared bidisperse granular flows at large size ratios.

Although this paper demonstrates that layering is driven by shear, occurs at large size ratios ($R \gtrsim 3$) and results in a structure in which large particles avoid direct contact, much remains to be understood. Open questions include the mechanisms that cause layering, and the characterisation of the parameter regimes in which it occurs, including how prevalent it is in more polydisperse flows. Moreover, the alignment of large particles and organisation into discrete layers significantly alter both the flow rheology and dilatancy (figure 6). This may have important consequences for the dynamics of bidisperse flows. Understanding the causes and consequences of layering will require further experimental, numerical and theoretical investigation.

To model the steady-state concentration profiles in a continuum framework, a bidirectional segregation flux has been introduced. This must be at least cubic in ϕ^s to allow for a sign change at ϕ_n^s , although it may have a more complex dependence on ϕ^s . The introduction of a root in the segregation flux at $\phi^s = \phi_n^s$ allows the model to capture the reversal in the direction of segregation as well as the approximately uniform segregation

states. This formulation provides a natural extension to larger size ratios of the cubic flux suggested by Gajjar & Gray (2014), originally proposed to model the asymmetry in the segregation rates between small and large particles. The segregation flux (5.2) therefore reconciles the conventional segregation behaviour at $R \lesssim 3$, with the qualitatively different behaviour at larger size ratios. A linear dependence on shear rate and inverse dependence on the pressure enters the segregation flux as a multiplicative prefactor as in Trehela *et al.* (2021). The model is in good quantitative agreement with the results of the DEM simulations at $R = 3$ and $R = 6$ over the full range of small-particle fractions (figures 14 and 15). Further comparison of the model predictions at slope angles of 23° and 27° in figure 17, corresponding to inertial numbers of $I = 0.09$ and 0.24 in monodisperse flows for the grains considered here, indicates that the model can be applied over much of the dense inertial regime, despite the shear rate and pressure dependence of the flux only previously being verified in the intruder limits up to a size ratio $R = 4$ (Trehela *et al.* 2021).

Despite the good agreement with the concentration profiles over a range of slope angles and small-particle fractions, a model in the proposed form cannot capture all of the features of segregation at large size ratios. In particular, a constant solids volume fraction, Φ , has been assumed across the flow. This is a reasonable simplifying assumption in the present work, but at larger size ratios packing effects and feedback of the particle-size distribution on the rheology, and hence on the dilatancy, may become more significant and cannot be neglected. One example is the transition towards spontaneous percolation (also known as free-sifting) which is the migration of the small particles through a matrix of large particles even in the absence of shear. This occurs for low small-particle fractions at size ratios $R \gtrsim 6.5$ (Dodds 1980). Description of segregating flows of this kind necessitates a change in the solids volume fractions, since the small particles are simply filling voids between large particles. In this regime, the velocity at which small particles percolate is insensitive to shear rate (Gao *et al.* 2024) whereas it is linear in the shear rate for $R \lesssim 6.5$. This indicates that the form of the segregation flux must change in regimes where spontaneous percolation occurs, perhaps by incorporating a term that is independent of the shear rate.

Supplementary movies. Supplementary movies are available at <https://doi.org/10.1017/jfm.2026.11227>.

Acknowledgements. The authors acknowledge valuable discussions about layering and segregation with J. Monti and J. Lechman at Sandia National Laboratories.

Funding. C.G.J. and J.M.N.T.G. acknowledge funding from Natural Environment Research Council (NERC) grants NE/X00029X/1 and NE/X013936/1/. J.M.N.T.G. was supported by a Royal Society Wolfson Research Merit Award (WM150058) and an EPSRC Established Career Fellowship (EP/M022447/1).

Declaration of interests. The authors report no conflict of interest.

Data availability statement. The coarse-grained small-particle concentration ϕ^s , velocity u and RDF $g(r)$ obtained from DEM simulations and used to create plots in this paper are archived at Zenodo (<https://doi.org/10.5281/zenodo.17910940>).

Appendix A. Table of DEM simulations

The size ratio R , small-particle fraction $\bar{\phi}^s$ and slope angle θ used in all DEM simulations performed on an inclined plane in this paper are provided in table 2. All Lees–Edwards simulations in this paper have $R = 6$, small-particle concentration $\phi^s = 0.5$ and volume fraction $\Phi = 0.63$, except for those shown in figure 10, where Φ is varied and takes values 0.54, 0.57, 0.6 and 0.63.

R	$\overline{\phi^s}$	θ
2	0.7	25°
3, 6	0.1, 0.2, 0.3, 0.4, 0.5, 0.6, 0.7, 0.8, 0.9	25°
4	0.8, 0.9, 1 ⁻	25°
5	0.8	25°
7	0.5, 0.6	25°
5.2, 5.4, 5.6	0.7	25°
3.6, 3.8, 4, 4.2, 4.4, 4.6, 4.8	1 ⁻	25°
3	0.2, 0.4, 0.7	23°
3	0.3, 0.6, 0.8	27°
6	0.1, 0.2, 0.9	23°
6	0.2, 0.5, 0.7	27°

Table 2. Size ratio R , small-particle fraction $\overline{\phi^s}$ and slope angle θ of all DEM simulations performed on an inclined plane. The notation $\overline{\phi^s} = 1^-$ denotes the limit of a single large intruder. The mass of flowing grains per unit planar area is fixed at $60\rho_s d^s$ in all simulations.

Appendix B. Coarse-graining

The continuum concentration fields ϕ^v are constructed using the method of coarse-graining (Tunuguntla *et al.* 2016). The z profiles of the small- and large-particle volume fraction fields Φ^v are computed directly using the one-dimensional coarse-graining formula (see Barker, Zhu & Sun 2022)

$$\Phi^v(t, z) = \frac{1}{L_x L_y} \sum_{i \in S^v} V_i \frac{1}{\sqrt{2\pi}c} \exp\left(-\frac{(z - z_i(t))^2}{2c^2}\right) H(3c - |z - z_i(t)|). \quad (\text{B1})$$

Here L_x and L_y are the lengths of the box in the x and y directions respectively, S^v is the set of particles of species v , $V_i = (\pi/6)d_i^3$ is the volume of particle i which has diameter d_i and $z_i(t)$ is its z coordinate at time t .

Two values for the coarse-graining width c are used in this paper, $c = 0.2d^s$ and $c = 0.8d^l$. Both values are chosen from plateaus on which continuum fields are insensitive to c (Tunuguntla *et al.* 2016). Evidence for these plateaus is presented in figures 19(a) and 19(b) for $R = 3$ and $R = 6$, respectively. When seeking to model the segregation present in figure 2, $c = 0.8d^l$ is chosen to suppress oscillations due to particle-scale layering, as shown in figure 19(c–f). When seeking to resolve the layers, a smaller width of $c = 0.2d^s$ is used. The vertical positions of these layers may be determined from the definition in § 3, and the maximum and minimum layer heights are marked on the plots. Since the Gaussian function extends to infinity, to ensure it has compact support a finite cut-off of $3c$ is applied, enforced by the Heaviside step function H .

The concentration fields are obtained from Φ^v by

$$\phi^v = \frac{\Phi^v}{\Phi}, \quad (\text{B2})$$

where $\Phi = \Phi^s + \Phi^l$ is the total solids volume fraction. For the inclined-plane simulations compared with the segregation model, time-averaging is performed on ϕ^v once a steady state is reached, using 10 different measurements spaced at intervals of $100(d^s/g)^{1/2}$. The free surface is defined as the point where the time-averaged total solids volume fraction Φ falls below 0.1. To minimise the influence of the rigid base at $z = 0$ on the concentration profiles used for fitting the segregation model, coarse-graining begins a distance $1.5d^l$ above the base.

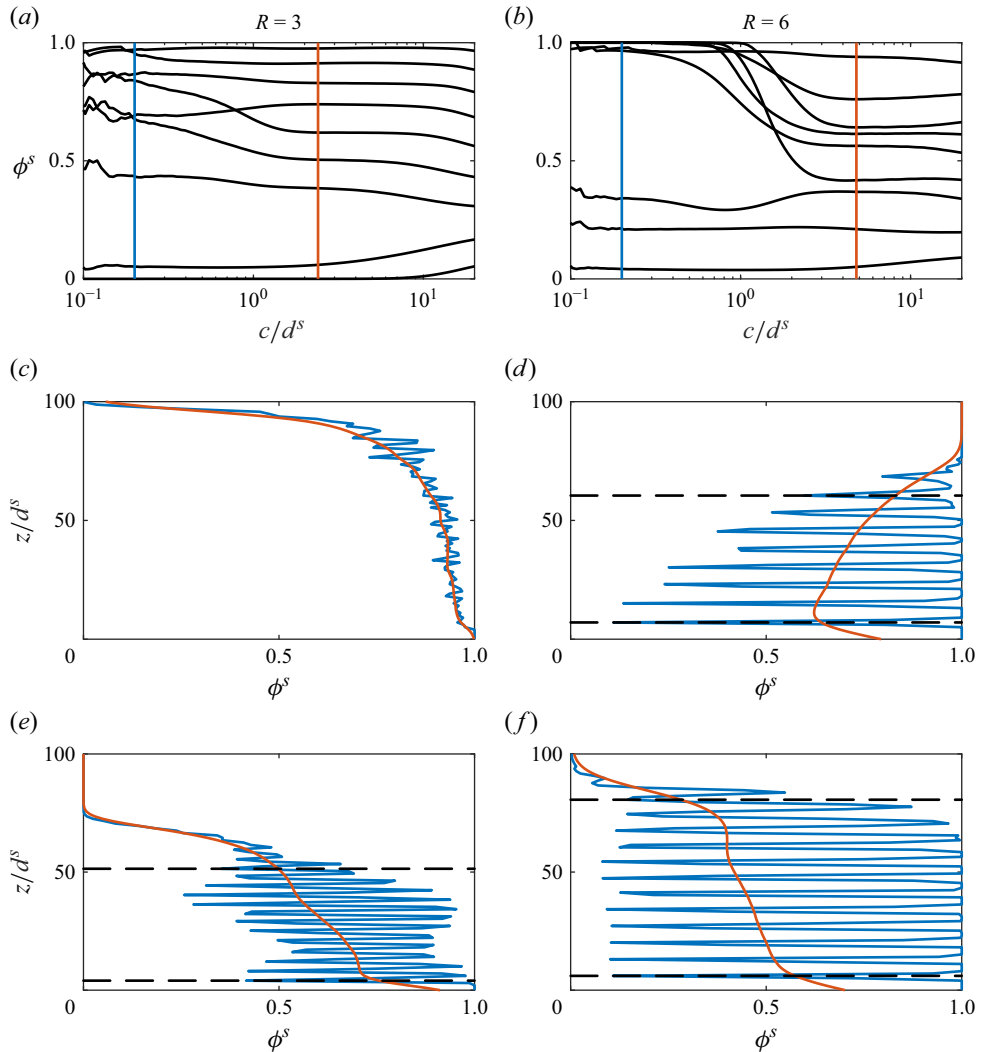


Figure 19. Small-particle concentration ϕ^s as a function of coarse-graining width c for size ratios (a) $R = 3$ and (b) $R = 6$. Each of the simulations in figure 2 are represented, with ϕ^s computed at height $z = 50d^s$. The vertical lines mark $c = 0.2d^s$ (blue) and $c = 0.8d^l$ (orange), the values used to construct continuum fields. Vertical profiles $\phi^s(z)$ for (c) $R = 3$ and (d) $R = 6$. The profiles are coarse-grained with widths $c = 0.2d^s$ (blue) and $0.8d^l$ (orange). The simulations are from a plane inclined at 25° with $\bar{\phi}^s = 0.8$. (e,f) The corresponding simulations with $\bar{\phi}^s = 0.4$. Black dashed lines in (d–f) indicate the maximum and minimum vertical positions of layers, defined as in § 3.

The small coarse-graining width of $c = 0.2d^s$ leads to sensitivity in the height of the free surface to particle-scale fluctuations. To mitigate this, the free surface in figure 5(c) is defined as the curve where $\Phi = 0.2$, when coarse-grained with $c = 4.8d^l$.

In the Lees–Edwards simulations, variation in the vorticity, y , direction is also considered. The small and large volume fractions are computed using the two-dimensional coarse-graining formula

$$\Phi^v(t, y, z) = \frac{1}{L_x} \sum_{i \in S^v} V_i \frac{1}{2\pi c^2} \exp\left(-\frac{r_i^2}{2c^2}\right) H(3c - r_i), \quad (\text{B3})$$

where

$$r_i = \sqrt{(y - y_i(t))^2 + (z - z_i(t))^2} \quad (\text{B4})$$

and $y_i(t)$ is the y coordinate of particle i at time t . A coarse-graining width of $c = 0.2d^s$ is used for the Lees–Edwards simulations. The concentration fields are then obtained using (B2).

The velocity field $\mathbf{u}(t, z)$ is obtained using

$$\mathbf{u}(t, z) = \frac{1}{L_x L_y \Phi(t, z)} \sum_i V_i \mathbf{u}_i \frac{1}{\sqrt{2\pi}c} \exp\left(-\frac{(z - z_i(t))^2}{2c^2}\right) H(3c - z_i), \quad (\text{B5})$$

where \mathbf{u}_i is the velocity of particle i and the sum is taken over all particles.

REFERENCES

- BAGNOLD, R.A. 1954 Experiments on gravity-free dispersion of large solid spheres in a Newtonian fluid under shear. *Proc. R. Soc. Lond. A* **225**, 49–63.
- BANCROFT, R.S.J. & JOHNSON, C.G. 2021 Drag, diffusion and segregation in inertial granular flows. *J. Fluid Mech.* **924**, A3.
- BARKER, T., ZHU, C. & SUN, J. 2022 Exact solutions for steady granular flow in vertical chutes and pipes. *J. Fluid Mech.* **930**, A21.
- BRIDGWATER, J. 1980 Self-diffusion coefficients in deforming powders. *Powder Technol.* **25**, 129–131.
- BRIDGWATER, J., FOO, W. & STEPHENS, D. 1985 Particle mixing and segregation in failure zones - theory and experiment. *Powder Technol.* **41**, 147–158.
- CAI, R., XIAO, H., ZHENG, J. & ZHAO, Y. 2019 Diffusion of size bidisperse spheres in dense granular shear flow. *Phys. Rev. E* **99**, 032902.
- CAMPBELL, C.S. 1997 Self-diffusion in granular shear flows. *J. Fluid. Mech* **348**, 85–101.
- CHASSAGNE, R. 2021 Discrete and continuum modelling of grain size segregation: application to bedload transport. PhD thesis, Univ. Grenoble Alpes.
- CHIALVO, S., SUN, J. & SUNDARESAN, S. 2013 Bridging the rheology of granular flows in three regimes. *Phys. Rev. E* **85**, 021305.
- CUNDALL, P.A. & STRACK, O.D.L. 1979 A discrete numerical model for granular assemblies. *Geotechnique* **29**, 29–44.
- DODDS, J.A. 1980 The porosity and contact points in multicomponent random sphere packings calculated by a simple statistical geometric model. *J. Colloid Interface Sci.* **77**, 317–327.
- DOLGUNIN, V.N. & UKOLOV, A.A. 1995 Segregation modelling of particle rapid gravity flow. *Powder Technol.* **83**, 95–103.
- DUAN, Y., UMBANHOWER, P.B., OTTINO, J.M. & LUEPTOW, R.M. 2021 Modelling segregation of bidisperse granular mixtures varying simultaneously in size and density for free surface flows. *J. Fluid Mech.* **918**, A20.
- EVANS, D.J. & MORRIS, G.P. 2007 *Statistical Mechanics of Nonequilibrium Liquids*. ANU Press.
- FAN, Y. & HILL, K.M. 2011 Theory for shear-induced segregation of dense granular mixtures. *New J. Phys.* **13** (9), 095009.
- FAN, Y., SCHLICK, C.P., UMBANHOWAR, P.B., OTTINO, J.M. & LUEPTOW, R.M. 2014 Modelling size segregation of granular materials: the roles of segregation, advection and diffusion. *J. Fluid Mech.* **741**, 252–279.
- FÉLIX, G. & THOMAS, N. 2004a Relation between dry granular flow regimes and morphology of deposits: formation of levées in pyroclastic deposits. *Earth Planet. Sci. Lett.* **221**, 197–213.
- FÉLIX, G. & THOMAS, N. 2004b Evidence of two effects in the size segregation process in dry granular media. *Phys. Rev. E* **70** (5), 051307.
- FRAYSSE, N., D'ORTONA, U. & THOMAS, N. 2024 Interaction between two large particles in a dry granular shear flow. *Phys. Rev. E* **109**, 064903.
- FRY, A.M., UMBANHOWAR, P.B., OTTINO, J.M. & LUEPTOW, R.M. 2019 Diffusion, mixing, and segregation in confined granular flows. *AIChE J.* **65**, 875–881.
- GAJJAR, P. & GRAY, J.M.N.T. 2014 Asymmetric flux models for particle-size segregation in granular avalanches. *J. Fluid Mech.* **757**, 297–329.
- GAO, S., OTTINO, J.M., LUEPTOW, R.M. & UMBANHOWER, P.B. 2024 Vertical velocity of a small sphere in a sheared granular bed. *Phys. Rev. Res.* **6**, L022015.

- GDR-MiDi 2004 On dense granular flows. *Eur. Phys. J. E* **14**, 341–365.
- GOLICK, L.A. & DANIELS, K.E. 2009 Mixing and segregation rates in sheared granular materials. *Phys. Rev. E* **80** (4), 042301.
- GRAY, J.M.N.T. 2018 Particle segregation in dense granular flows. *Annu. Rev. Fluid Mech.* **50**, 407–433.
- GRAY, J.M.N.T. & ANCEY, C. 2015 Particle-size and particle-density segregation in granular avalanches. *J. Fluid Mech.* **779**, 622–668.
- GRAY, J.M.N.T. & CHUGUNOV, V.A. 2006 Particle-size segregation and diffusive remixing in shallow granular avalanches. *J. Fluid Mech.* **569**, 365–398.
- GRAY, J.M.N.T. & THORNTON, A.R. 2005 A theory for particle size segregation in shallow granular free-surface flows. *Proc. R. Soc. A* **461**, 1447–1473.
- GUILLARD, F., FORTERRE, Y. & POULIQUEN, O. 2016 Scaling laws for segregation forces in dense sheared granular flows. *J. Fluid Mech.* **807**, R1.
- HILL, K.M. & TAN, S.D. 2014 Segregation in dense sheared flows: gravity, temperature gradients, and stress partitioning. *J. Fluid Mech.* **756**, 54–88.
- IVERSON, R.M. & VALLANCE, J.W. 2001 New views of granular mass flows. *Geology* **29** (2), 115–118.
- JING, L., OTTINO, J.M., LUEPTOW, R.M. & UMBANHOWAR, P.B. 2020 Rising and sinking intruders in dense granular flows. *Phys. Rev. Res.* **2**, 022069.
- JING, L., OTTINO, J.M., LUEPTOW, R.M. & UMBANHOWAR, P.B. 2021 A unified description of gravity- and kinematics-induced segregation forces in dense granular flows. *J. Fluid Mech.* **925**, A29.
- JING, L., OTTINO, J.M., LUEPTOW, R.M. & UMBANHOWAR, P.B. 2022 Drag force in granular shear flows: regimes, scaling laws and implications for segregation. *J. Fluid Mech.* **948**, A24.
- JOHNSON, C.G., KOKELAAR, B.P., IVERSON, R.M., LOGAN, M., LAHUSEN, R.G. & GRAY, J.M.N.T. 2012 Grain-size segregation and levee formation in geophysical mass flows. *J. Geophys. Res.* **117**, F01032.
- JOP, P., FORTERRE, Y. & POULIQUEN, O. 2005 Crucial role of sidewalls in granular surface flows: consequences for the rheology. *J. Fluid Mech.* **541**, 167–192.
- JOP, P., FORTERRE, Y. & POULIQUEN, O. 2006 A constitutive relation for dense granular flows. *Nature* **44**, 727–730.
- KHAREL, P. & ROGNON, P. 2018 Shear-induced diffusion in non-local granular flows. *Europhys. Lett.* **124**, 24002.
- LEES, A.W. & EDWARDS, S.F. 1972 The computer study of transport processes under extreme conditions. *J. Phys.* **C5**, 1921–1928.
- LLOYD, H.A., MAGUIRE, E.S.F., MISTRY, D., REYNOLDS, G.K., JOHNSON, C.G. & GRAY, J.M.N.T. 2025 On the formation of super-stable granular heaps. *J. Fluid Mech.* **1002**, A27.
- MAGUIRE, E.S.F., BARKER, T., RAUTER, M., JOHNSON, C.G. & GRAY, J.M.N.T. 2024 Particle-size segregation patterns in a partially filled triangular rotating drum. *J. Fluid Mech.* **979**, A40.
- MALBRANCHE, N., CHAKRABORTY, B. & MORRIS, J.F. 2023 Shear thickening in dense bidisperse suspensions. *J. Rheol.* **67**, 91–104.
- MARKS, B., ROGNON, P. & EINAV, I. 2012 Grainsize dynamics of polydisperse granular segregation down inclined planes. *J. Fluid Mech.* **690**, 499–511.
- MIDDLETON, G.V. 1970 Experimental studies related to problems of flysch sedimentation. In *Flysch Sedimentology in North America* (ed. J. Lajoie), pp. 253–272. Business and Economics Science Ltd.
- ROCHA, F.M., JOHNSON, C.G. & GRAY, J.M.N.T. 2019 Self-channelization and levee formation in monodisperse granular flows. *J. Fluid Mech.* **876**, 591–641.
- ROGNON, P.G., ROUX, J.N., NAAIM, M. & CHEVOIR, F. 2007 Dense flows of bidisperse assemblies of disks down an inclined plane. *Phys. Fluids* **19**, 058101.
- ROUSSEAU, H., CHAUCHAT, J. & FREY, P. 2022 Experiments on a single large particle segregating in bedload transport. *Phys. Rev. Fluids* **7**, 064305.
- SANTL, M., ILIC, I., VRECER, F. & BAUMGARTNER, S. 2012 A compressibility and compactibility study of real tableting mixtures: the effect of granule particle size. *Acta Pharmaceut.* **62**, 325–340.
- SAVAGE, S.B. & DAI, R. 1993 Studies of granular shear flows wall slip velocities, ‘layering’ and self-diffusion. *Mech. Matter* **16**, 225–238.
- SAVAGE, S.B. & LUN, C.K.K. 1988 Particle size segregation in inclined chute flow of dry cohesionless granular solids. *J. Fluid Mech.* **189**, 311–335.
- SCHULZE, D. 2008 *Powders and Bulk Solids: Behaviour, Characterization, Storage and Flow*, p. 511. Springer.
- SILBERT, L.E., ERTAS, D., GREST, G.S., HALSEY, T.C., LEVINE, D. & PLIMPTON, S.J. 2001 Granular flow down an inclined plane: Bagnold scaling and rheology. *Phys. Rev. E* **64**, 051302.
- SILBERT, L.E., GREST, G.S., PLIMPTON, S.J. & LEVINE, D. 2002 Boundary effects and self-organization in dense granular flows. *Phys. Fluids* **14**, 2637–2646.

- SRIVASTAVA, I., ROBERTS, S.A., CLEMMER, J.T., SILBERT, L.E., LECHMAN, J.B. & GREY, G.S. 2021 Jamming of bidisperse frictional spheres. *Phys. Rev. Res.* **3**, L032042.
- STARON, L. & PHILLIPS, J.C. 2015 Stress partition and micro-structure in size-segregating granular flows. *Phys. Rev. E* **92**, 022210.
- THOMAS, N. 2000 Reverse and intermediate segregation of large beads in dry granular media. *Phys. Rev. E* **62**, 961–974.
- THOMAS, N. & D'ORTONA, U. 2018 Evidence of reverse and intermediate size segregation in dry granular flows down a rough incline. *Phys. Rev. E*.
- THOMPSON, A.P., *et al.* 2022 LAMMPS - a flexible simulation tool for particle-based materials modeling at the atomic, meso, and continuum scales. *Comput. Phys. Commun.* **271**, 108171.
- THORNTON, A.R., WEINHART, T., LUDING, S. & BOKHOVE, O. 2012 Modeling of particle size segregation: calibration using the discrete particle method. *Intl J. Mod. Phys. C* **23**, 1240014.
- TREWHELA, T., ANCEY, C. & GRAY, J.M.N.T. 2021 An experimental scaling law for particle-size segregation in dense granular flows. *J. Fluid Mech.* **916**, A55.
- TRIPATHI, A. & KHAKAR, D.V. 2013 Density difference-driven segregation in a dense granular flow. *J. Fluid. Mech.* **717**, 643–669.
- TRIPATHI, A. & KHAKHAR, D.V. 2011 Rheology of binary granular mixtures in the dense flow regime. *Phys. Fluids* **23**, 113302.
- TUNUGUNTLA, D.R., BOKHOVE, O. & THORNTON, A.R. 2014 A mixture theory for size and density segregation in shallow granular free-surface flows. *J. Fluid. Mech.* **749**, 99–112.
- TUNUGUNTLA, D.R., THORNTON, A.R. & WEINHART, T. 2016 From discrete elements to continuum fields: extension to bidisperse systems. *Comput. Part. Mech.* **3**, 349–365.
- TUNUGUNTLA, D.R., WEINHART, T. & THORNTON, A.R. 2017 Comparing and contrasting size-based particle segregation models. *Comput. Part. Mech.* **4**, 387–405.
- UMBANHOWER, P.B., LUEPTOW, R.M. & OTTINO, J.M. 2019 Modeling segregation in granular flows. *Annu. Rev. Chem. Biomol. Engng* **10**, 129–153.
- UTTER, B. & BEHRINGER, R.P. 2004 Self-diffusion in dense granular shear flows. *Phys. Rev. E* **69**, 031308.
- VAN DER VAART, K., GAJJAR, P., EPELY-CHAUVIN, G., ANDREINI, N., GRAY, J.M.N.T. & ANCEY, C. 2015 Underlying asymmetry within particle size segregation. *Phys. Rev. Lett.* **114**, 238001.
- VAN DER VAART, K., VAN SCHROJENSTEIN LANTMAN, M.P., WEINHART, T., LUDING, S., ANCEY, C. & THORNTON, A.R. 2018 Segregation of large particles in dense granular flows: a granular Saffman effect? *Phys. Rev. Fluids* **3**, 074303.
- WEINHART, T., HARTKEMP, R., THORNTON, A.R. & LUDING, S. 2013 Coarse-grained local and objective continuum description of three-dimensional granular flows down an inclined surface. *Phys. Fluids* **25**, 070605.
- WIACEK, J. 2016 Geometrical parameters of binary granular mixtures with size ratio and volume fraction: experiments and DEM simulations. *Granul. Matter* **8**, 42.
- WIEDERSEINER, S., ANDREINI, N., EPELY-CHAUVIN, G., MOSER, G., MONNEREAU, M., GRAY, J.M.N.T. & ANCEY, C. 2011 Experimental investigation into segregating granular flows down chutes. *Phys. Fluids* **23**, 013301.
- WILKINSON, D.R. & EDWARDS, S.F. 1982 Spontaneous interparticle percolation. *Proc. R. Soc. A* **381**, 33–51.